JCB

Article

Mechanism of Stx17 recruitment to autophagosomes via IRGM and mammalian Atg8 proteins

Suresh Kumar,[1,2] Ashish Jain,[3] Farzin Farzam,[4] Jingyue Jia,[1,2] Yuexi Gu,[1,2] Seong Won Choi,[1,2] Michal H. Mudd,[1,2] Aurore Claude-Taupin,[1,2] Michael J. Wester,[5] Keith A. Lidke,[4] Tor-Erik Rusten,[3] and Vojo Deretic[1,2]

[1]Autophagy Inflammation and Metabolism Center of Biomedical Research Excellence and [2]Department of Molecular Genetics and Microbiology, University of New Mexico Health Sciences Center, Albuquerque, NM
[3]Department of Molecular Cell Biology, Centre for Cancer Biomedicine, University of Oslo and Institute for Cancer Research, The Norwegian Radium Hospital, Oslo, Norway
[4]Department of Physics and Astronomy and [5]Department of Mathematics and Statistics, University of New Mexico, Albuquerque, NM

Autophagy is a conserved eukaryotic process with metabolic, immune, and general homeostatic functions in mammalian cells. Mammalian autophagosomes fuse with lysosomes in a SNARE-driven process that includes syntaxin 17 (Stx17). How Stx17 translocates to autophagosomes is unknown. In this study, we show that the mechanism of Stx17 recruitment to autophagosomes in human cells entails the small guanosine triphosphatase IRGM. Stx17 directly interacts with IRGM, and efficient Stx17 recruitment to autophagosomes requires IRGM. Both IRGM and Stx17 directly interact with mammalian Atg8 proteins, thus being guided to autophagosomes. We also show that Stx17 is significant in defense against infectious agents and that Stx17–IRGM interaction is targeted by an HIV virulence factor Nef.

Introduction

Autophagy is a collection of intracellular homeostatic processes with roles in cytoplasmic quality control and metabolism impacting a broad spectrum of degenerative, inflammatory, and infectious diseases (Mizushima et al., 2008). The best-studied form of autophagy, macroautophagy, depends on the autophagy-related gene (Atg) factors in yeast, where this system has been genetically delineated (Mizushima et al., 2011). The many similarities of the core Atg machinery in yeast and mammalian cells (Mizushima et al., 2011) are complemented by qualitative and quantitative differences between how mammalian and yeast cells execute autophagy. This extends but is not limited to an expanding spectrum of mammalian receptors (Birgisdottir et al., 2013; Rogov et al., 2014; Wei et al., 2017) and receptor regulators (Kimura et al., 2016) for selective autophagy as well as the dominant role in mammalian cells of ubiquitin (Khaminets et al., 2016) and galectin (Thurston et al., 2012; Chauhan et al., 2016; Kimura et al., 2017) tags enabling recognition of autophagy targets. Perhaps the most intriguing differences are the roles of unique regulators of autophagy such as, among prominent others recognized early on as associated with genetic predispositions to diseases (Wellcome Trust Case Control Consortium, 2007), the immunity-related GTPase M (IRGM), which bridges the immune system and the core Atg machinery to control autophagy in human cells (Singh et al., 2006, 2010; Chauhan et al., 2015).

The role of the Atg-conjugating system, which leads to C-terminal lipidation of yeast Atg8 and its paralogs in mammals, in autophagosome formation has recently been questioned (Nishida et al., 2009; Nguyen et al., 2016; Tsuboyama et al., 2016), emphasizing instead its role in autophagosomal–lysosomal fusion (Nguyen et al., 2016; Tsuboyama et al., 2016). The number and complexity of mammalian Atg8s factors (mAtg8s: LC3A, LC3B, LC3C, GABARAP, GABARAPL1, and GABARAPL2; Weidberg et al., 2010), which are the substrate for the Atg conjugation machinery that lipidates the C-terminal Gly residues of all Atg8s after processing by the family of mammalian Atg4 proteases (Fujita et al., 2008; Fernández and López-Otín, 2015), exceeds the single yeast Atg8 homologue. Whereas LC3B and yeast Atg8 are often equated in recognizing the LC3-interaction region (LIR) or Atg8-interacting motif (AIM; Pankiv et al., 2007; Noda et al., 2010; Birgisdottir et al., 2013; Popelka and Klionsky, 2015) on receptors for selective autophagy, mAtg8s have additional functions (Sanjuan et al., 2007; Weidberg et al., 2010; Alemu et al., 2012; Nguyen et al., 2016; Tsuboyama et al., 2016) that are not completely understood. Unlike what is believed to be the case in yeast (Xie et al., 2008), inactivation of all six mAtg8s (Nguyen et al., 2016) or the components of the Atg conjugation machinery (Tsuboyama et al., 2016) does not prevent the formation of autophagosomes (although it affects their size) as it does in yeast (Xie et al., 2008), but instead precludes (Nguyen et al., 2016) or significantly delays (Tsuboyama et al., 2016) their fusion with lysosomes.

Exactly how autophagosomes mature in mammalian cells into autolysosomes, whether through fusion with the dispersed late endosomal and lysosomal organelles (Itakura et al., 2012; Tsuboyama et al., 2016) or progress to other terminal structures

Correspondence to Vojo Deretic: vderetic@salud.unm.edu

The Rockefeller University Press
J. Cell Biol. Vol. 217 No. 3 997–1013
https://doi.org/10.1083/jcb.201708039

(Zhang et al., 2015; Kimura et al., 2017), and how this compares with the delivery of autophagosomes to the single yeast vacuole (Liu et al., 2016) despite recent advances (Itakura et al., 2012; Hamasaki et al., 2013; Guo et al., 2014; Diao et al., 2015; McEwan et al., 2015; Nguyen et al., 2016; Wang et al., 2016; Wijdeven et al., 2016) is not fully understood. One of the key known events during mammalian autolysosome formation is the acquisition by autophagosomes (Itakura et al., 2012; Hamasaki et al., 2013; Takáts et al., 2013; Arasaki et al., 2015; Diao et al., 2015; Tsuboyama et al., 2016) of the Q_a-SNARE syntaxin 17 (Stx17; Steegmaier et al., 2000), heralding progression of nascent autophagosomal organelles toward the autophagosome–lysosome fusion (Itakura et al., 2012). Stx17, which plays several potentially diverse roles (Itakura et al., 2012; Hamasaki et al., 2013; Arasaki et al., 2015; McLelland et al., 2016), once recruited to autophagosomes forms a trans-SNARE complex by pairing with the R-SNAREs (e.g., VAMP8; Furuta et al., 2010; Itakura et al., 2012; Wang et al., 2016) located within the late endosomal/lysosomal membranes (Jahn and Scheller, 2006). To complete the four-helix SNARE bundle necessary to execute membrane fusion (Jahn and Scheller, 2006), Stx17 forms complexes with the cytosolic Q_{bc}-SNARE SNAP-29 (Itakura et al., 2012; Diao et al., 2015). Stx17 furthermore interacts (Jiang et al., 2014; Takáts et al., 2014) with a multicomponent membrane tether known as the homotypic fusion and protein sorting (HOPS) tethering complex (Balderhaar and Ungermann, 2013; Solinger and Spang, 2013), which also acts as a Sec1-Munc18 protein and controls the status of trans-SNARE complexes, protecting the four-helix SNARE bundle normally disassembled by *N*-ethylmaleimide–sensitive factor (NSF)/αSNAP (Xu et al., 2010). Several factors, including ATG14L (Diao et al., 2015), PLEKHM1 (McEwan et al., 2015), EPG5 (Wang et al., 2016), and Rab-interacting lysosomal protein (RILP; Wijdeven et al., 2016), interact with and strengthen the Stx17–SNAP-29–VAMP8 complex often in conjunction with HOPS.

Although the acquisition of Stx17 by the autophagosomal membranes represents a pivotal step for autophagosomal fusion with lysosomes, the mechanism of Stx17 recruitment specifically to autophagosomes is unknown. It has been shown that Stx17 inserts into the autophagosomal membrane as a hairpin-type tail-anchored protein coming from the cytosol or other locales (Itakura et al., 2012). Recruitment of Stx17 to emerging autophagosomes is strongly influenced by the LC3 lipidation machinery (Tsuboyama et al., 2016). Nevertheless, how Stx17 recognizes and specifically translocates to autophagosomes is not known. In this study, we show that Stx17 translocation to autophagosomes in human cells is promoted by IRGM. Both Stx17 and IRGM interact directly with mAtg8s, and all three components are found in a common protein complex, which we term the autophagosome recognition particle (ARP) for delivery of Stx17 to appropriate membranes during autophagy.

Results

Stx17 directly interacts with mammalian Atg8s

Superresolution (SR) microscopy of endogenous LC3 in cells expressing GFP-Stx17 revealed an array of profiles representing different stages along the autophagosomal pathway (Figs. 1 A and S1, type I–VII profiles) and indicated a separation of <25 nm for 75% of the Stx17 and LC3 cluster centers within the arms of type I profiles representing advanced phagophores (Fig. 1, B and C). This proximity suggested the possibility of direct or very close interactions between Stx17 and LC3. Thus, we considered the simplest model that mammalian paralogs of yeast Atg8 (mAtg8s: LC3A, LC3B, LC3C, GABARAP, GABARAPL1, and GABARAPL2), e.g., LC3B as an mAtg8 commonly used to visualize autophagosomes, may play a role in controlling recruitment of Stx17 to conventional autophagosomes. We found endogenous Stx17 in protein complexes with mAtg8s (expressed as GFP fusions) prominently with LC3B and GABARAP (Figs. 1 D and S2 A). Using GST pulldown experiments, we determined that Stx17 directly binds LC3B and GABARAP (Fig. 1 E). We next examined the Stx17 sequence for the presence of potential LIR motifs and found two distinct candidates ($LIR1^{172–175}$ and $LIR2^{189–192}$; Fig. 2 A) within the SNARE region of Stx17, conforming both with the LIR motif rules (Birgisdottir et al., 2013) and accessibility within an intrinsically disordered region of a protein (Popelka and Klionsky, 2015). Related to the latter aspect, SNARE domains (which are subregions within respective SNARE proteins) when not in complexes with other factors can have an intrinsically disordered structure that eventually transitions from largely unstructured to an energetically favored four-helix complex during membrane fusion (Fasshauer et al., 1997). When we mutated the aromatic and aliphatic pocket–interacting residues within the candidate LIRs, Stx17LIR** (double Stx17 LIR mutant of $LIR1^{172WA–175LA}$ and $LIR2^{189FA–192LA}$) showed reduced ability relative to WT Stx17 (Stx17WT) to bind LC3B and GAB ARAP in coimmunoprecipitates (coIPs; Figs. 2 B and S2 B) and GST pulldowns (Fig. S2 C). Thus, Stx17 has an intrinsic capacity to bind mAtg8s.

Stx17 recruitment to autophagosomes when mAtg8 conjugation machinery is inactivated diminishes, albeit it is not completely abrogated (Tsuboyama et al., 2016). When we used the previously characterized NIH3T3 cells expressing dominant-negative $Atg4B^{C74A}$ (Fujita et al., 2008), which prevents lipidation of all mAtg8s, this significantly reduced GFP-Stx17's ability to form puncta as a measure of membrane association, quantified by high-content (HC) microscopy (Fig. 2 C). These observations pose a question of the form of mAtg8s that associate with Stx17. Both forms (lipidated and unlipidated) of LC3B were found in coIPs with Stx17 under basal conditions (Fig. 2 D). However, induction of autophagy by starvation increased LC3-II/LC3-I ratios in Flag-Stx17 immunoprecipitates (IPs; Fig. 2 D). Thus, induction of conventional autophagy by starvation partially redirected Stx17 to the LC3-II form.

We next tested the effects of LIR mutant Stx17 (Stx17LIR**) on the recruitment of Stx17 to autophagosomes by HC using a time-course approach. We observed a reduced overlap between $LC3^+$ profiles and GFP-Stx17LIR** relative to GFP-Stx17WT at 15–30-min time points after induction of autophagy by starvation (Figs. 2 E and S2 D). Thus, LIR mutations affected the kinetics of Stx17 recruitment to autophagosomes. Past 1 h, when Stx17 association with autophagosomes began to decline, the difference between Stx17WT and Stx17LIR** was lost. Thus, Stx17 LIRs are important for its recruitment but not for its cycling off the autolysosomes. Furthermore, we tested whether LIRs in Stx17 were important for selectivity of Stx17's presence on other organelles where Stx17 is known to partition

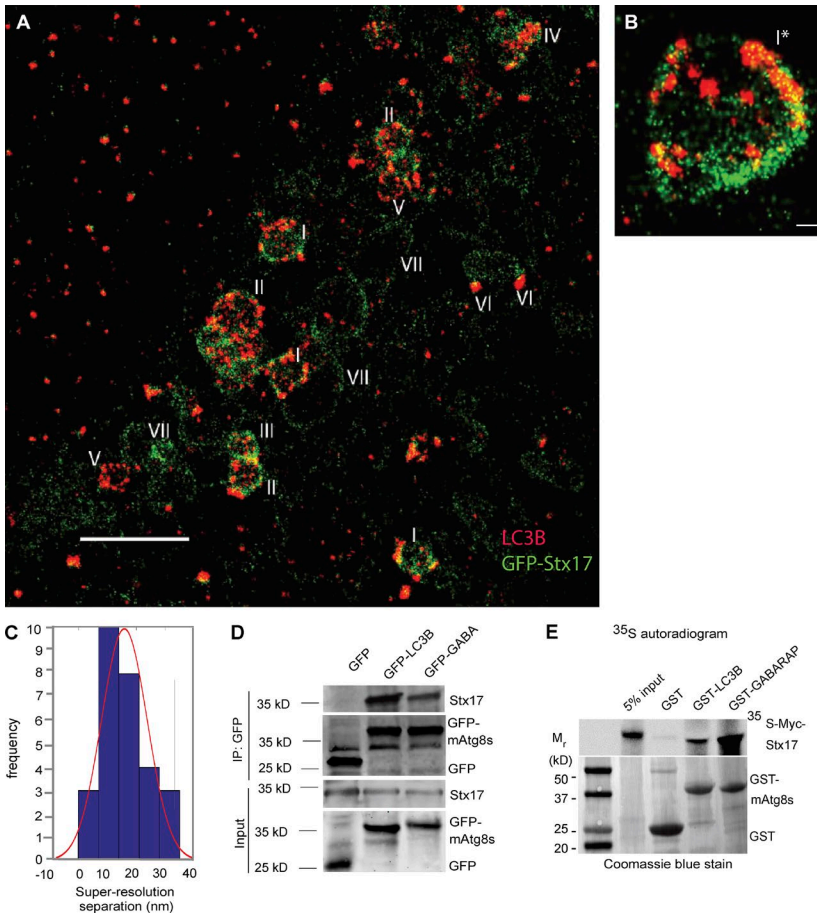

Figure 1. **Stx17 directly interacts with mAtg8s. (A)** SR microscopy of GFP-Stx17 and endogenous LC3. HeLa cells were transfected with GFP-Stx17 and induced for autophagy with pp242 for 2 h in the presence of bafilomycin A1 to allow for accumulation of intermediates, and then endogenous LC3 (rabbit anti-LC3) and GFP-Stx17 were sequentially imaged at 647 nm as detailed in the SR microscopy and analysis section in Materials and methods. Shown is a section of the whole-cell scan in Fig. S1. Pseudocolors: green, GFP-Stx17; red, endogenous LC3. A key to different autophagic profiles (marked I–VII) is given in the Fig. S1 legend. Bar, 1 µm. **(B)** Type I profile enlarged from Fig. S1, marked as "I*." Bar, 200 nm. **(C)** Graph showing a plot of center-to-center distances between LC3 and GFP-Stx17 cluster centroids from five type I profiles. **(D)** CoIP between GFP-LC3B or GFP-GABARAP and endogenous Stx17 in HEK293T cells. **(E)** GST pulldowns of radiolabeled [^{35}S]Myc-Stx17 with GST LC3B and GST GABARAP.

(Steegmaier et al., 1998, 2000; Itakura et al., 2012; Hamasaki et al., 2013; Arasaki et al., 2015). Stx17LIR** showed increased colocalization with TOM20 (mitochondria) and BiP (ER; Fig. S2, E and F). All of these observations are in keeping with the findings by Tsobuyama et al. (2016) indicating that a defect in mAtg8 conjugation system delays Stx17 recruitment.

IRGM interacts with Stx17

Albeit the Stx17 LIR** mutant showed reduced binding to LC3B (Fig. 2 B) and GABARAP (Fig. S2 B), there was some residual association between these mAtg8s and Stx17 in cells. In the course of our experiments with Stx17, we observed independently of the results in the previous section Stx17's propensity to colocalize (Fig. 3, A and B; and Fig. S2 G) with IRGM, an immunity-related GTPase implicated in the regulation of autophagy (Singh et al., 2006; Chauhan et al., 2015). Furthermore, association between Stx17 and IRGM was confirmed in coIPs between GFP-IRGM and FLAG-Stx17 (Fig. S2 H), reverse coIPs (Fig. S2 I), and coIP of endogenous IRGM with GFP-Stx17 (Fig. S2 J). Endogenous IRGM was found in complexes with Stx17 (as well as LC3; Figs. 3 C and S2 K). Stx17LIR** associated with IRGM (Fig. S2 L), suggesting that IRGM and Stx17 binding was not dependent on Stx17's association through its LIRs with mAtg8s.

Next, we tested whether the Stx17 recruitment function of IRGM could be separated from the previously reported function in the assembly of the core autophagy initiation factors (Chauhan et al., 2015). When IRGM^{S47N} mutant (corresponding with inactive GTPases; Singh et al., 2010) was tested, IRGM-Stx17 association was lost (Fig. 3, D and F). The same IRGM^{S47N} mutant did not lose its binding to Beclin1 (Fig. 3, E and F). Conversely, a different IRGM mutant, IRGM^{Kmut}, which cannot assemble ULK1, Beclin1, and ATG16L1 during autophagy initiation (Chauhan et al., 2015), still bound Stx17 (Fig. 3, G–I). Thus, IRGM's role in the assembly of the autophagy initiation complexes and its role in the recruitment of Stx17 to autophagosomes can be separated.

Association between GFP-Stx17 and FLAG-IRGM was enhanced upon induction of autophagy using the mTOR inhibitor pp242 (Fig. S2 M). Increased association between WT IRGM and Stx17 was observed in the presence of a non-hydrolyzable analogue of GTP (Fig. S2 N). Interactions between IRGM and Stx17 were also tested using a proximity biotinylation assay using a modified ascorbate peroxidase (APEX) probe APEX2 (Lam et al., 2015). This assay has been developed (Lam et al., 2015) to allow for in vivo analysis of protein–protein proximity whereby a fusion of APEX2 with one of the partners will permit biotinylation of its neighbor based on the short half-life and small labeling radius of <20 nm of the peroxidase reaction product of APEX with biotin phenol (biotin-phenoxyl radical; Rhee et al., 2013). IRGM was fused at its N terminus with APEX2, and transfected cells were incubated with biotin phenol. After biotinylation reaction (Lam et al., 2015), products in cell lysates were incubated with streptavidin beads, adsorbed proteins were eluted, and levels of endogenous Stx17 bound to and eluted from streptavidin beads were assessed by immunoblotting (Fig. S3 A). Expression of APEX2-IRGM resulted in increased biotinylation of endogenous Stx17 (Fig. S3 B), indicating close proximity of IRGM and Stx17 in the cells. Finally, direct Stx17-IRGM binding was demonstrated in GST pulldown assays (Fig. 3 J).

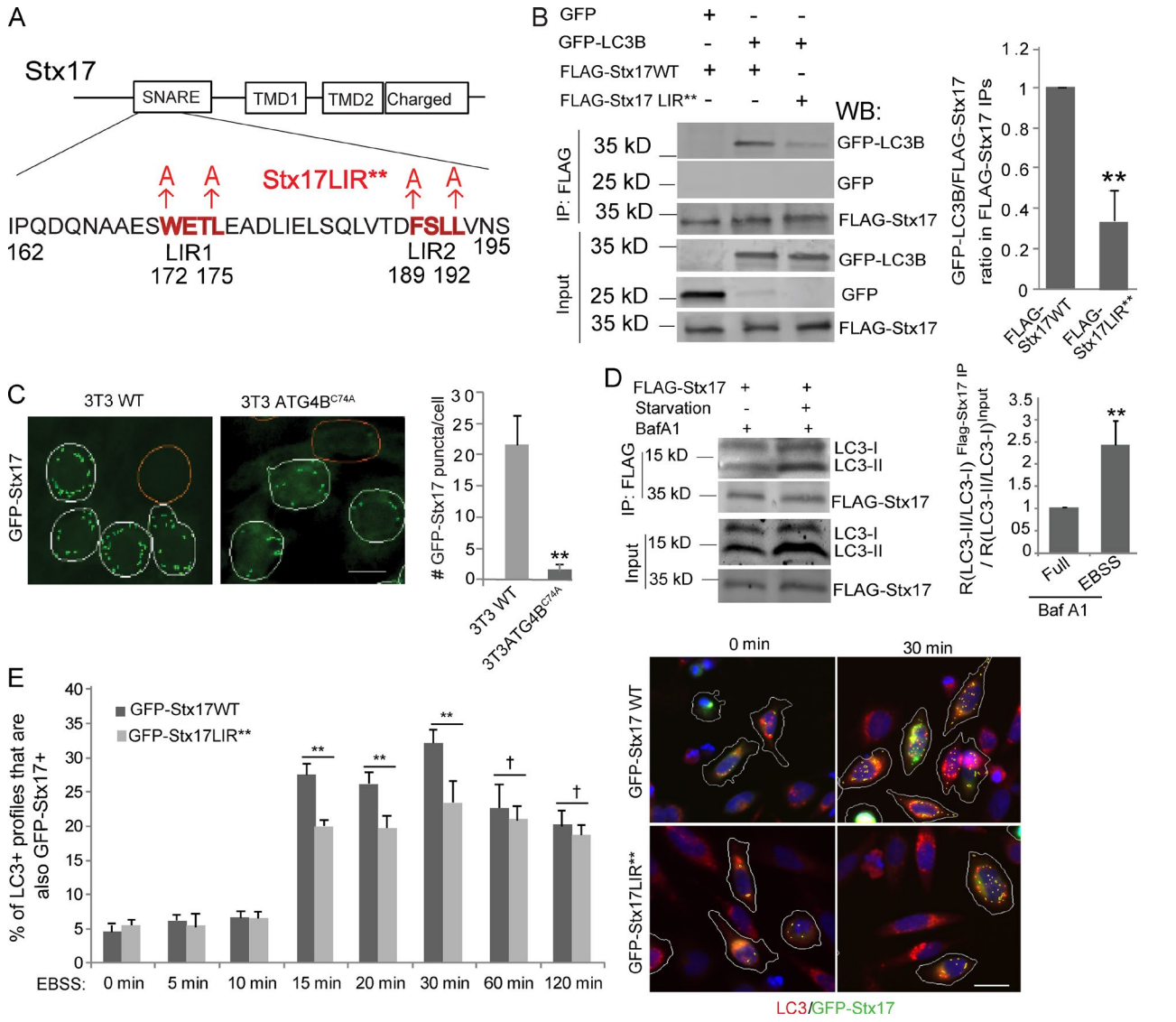

Figure 2. **Stx17 LIRs affect its recruitment to autophagosomes. (A)** Stx17 LIRs within the SNARE domain of Stx17. Two potential LIR motifs (172–175 WETL and 189–192 FSLL, red) were identified using bioinformatics within the Stx17 SNARE domain; key residues, W^{172}, I^{175}, F^{189}, and L^{192} were mutated to A (arrows; LIR**). **(B)** CoIP analysis and quantification of interactions between GFP-LC3B and WT and the double LIR mutant FLAG-Stx17 LIR** in 293T cells. In IP blots, GFP-LC3B and GFP sections were cropped to avoid IgG bands. Data indicate means ± SEM of intensities normalized to FLAG-Stx17 in FLAG IPs. WB, Western blot. **(C)** WT 3T3 and 3T3 cells stably expressing dominant-negative ATG4B^{C74A} were transfected with GFP-Stx17 and induced for autophagy (2-h EBSS), and then the number of GFP-Stx17 puncta per cell was quantified by HC microscopy. Masks: white, primary objects (cells); green puncta, number of valid Stx17 puncta; orange, rejected primary objects (cells). Data indicate means ± SEM (HC microscopy, >500 primary objects counted per well; minimum number of wells was four). **(D)** CoIP analysis of interactions between FLAG-Stx17 and endogenous LC3B in 293T cells treated with bafilomycin A1 under full and starvation (2-h EBSS) conditions. Data indicate means ± SEM of ratios between LC3-II and LC3-I intensities in FLAG-Stx17 IPs expressed relative (normalized) to LC3-II/LC3-I ratios in inputs. **(E)** HC microscopy analysis (time course) of HeLa cells transfected with GFP-Stx17WT and GFP-Stx17LIR** and incubated in starvation media (EBSS) for indicated periods. Data indicate means ± SEM. (B–E) **, $P < 0.01$; †, $P \geq 0.05$ ($n = 3$) *t* test (B–D) or ANOVA (E) from three independent experiments (>500 primary objects counted per well; minimum number of wells was 12). Right: HC microscopy images. Overlap (yellow masks) between LC3 and GFP-Stx17WT or GFP-Stx17LIR** at 0 min and 30 min after induction of autophagy using EBSS. Bars, 10 µm.

IRGM and Stx17 are on autophagic membranes

A question arose whether IRGM and Stx17 can be found on autophagosomal membranes before fusion with lysosomes. We separated intracellular membranes by subjecting sequentially fractionated 25,000-*g* (25K) pellets to floatation in OptiPrep gradients (Fig. 4 A) and found that Stx17 and IRGM were present in membrane fractions positive for LC3-II (Fig. 4 B, fraction 3). These fractions were devoid of LAMP2. The observed absence of LAMP2 in IRGM and LC3-II–positive fractions indicates that IRGM and Stx17 are on autophagic membranes before their fusion with lysosomes. Furthermore, we also observed colocalization between IRGM and Stx17 on LC3$^+$ profiles in cells induced for autophagy by pp242 in the presence of bafilomycin A1 (Fig. S3 C).

IRGM interacts with the Stx17 region required for translocation to autophagic membranes

We next mapped the region in Stx17 required for interactions with IRGM. Stx17 has a proposed hairpin structure formed by two trans-membrane domains (TMDs) containing glycine

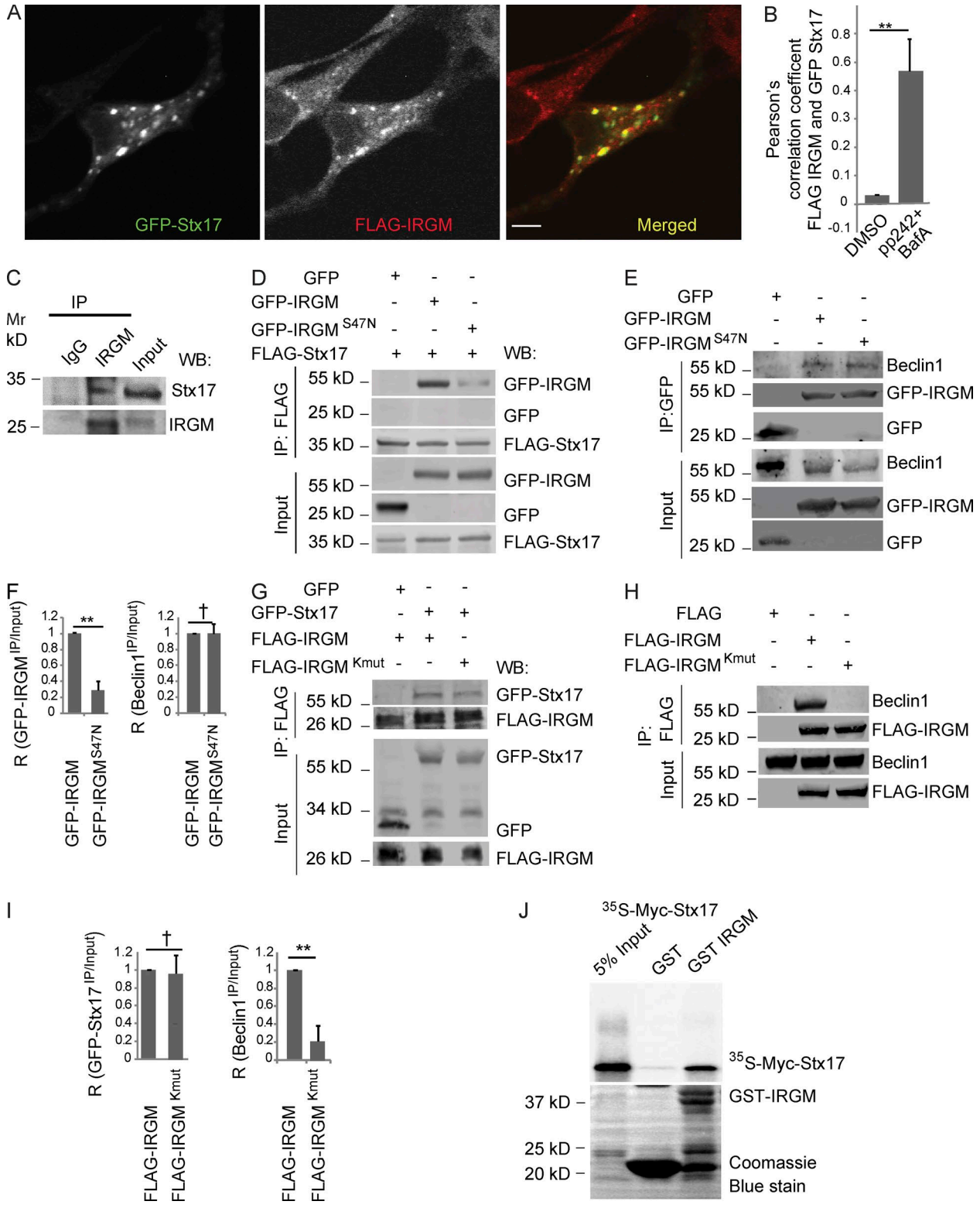

Figure 3. **Stx17 directly interacts with IRGM. (A)** Confocal microscopy analysis of GFP-Stx17 and FLAG-IRGM localization (yellow profiles in merged image reflect colocalization) in HeLa cells treated with pp242 and bafilomycin A1. Bar, 5 µm. **(B)** Graph showing Pearson's correlation coefficient (>20 cells) between FLAG-IRGM and GFP-Stx17. **(C)** CoIP analysis of interactions between endogenous IRGM and Stx17 in 293T cells. **(D)** CoIP analysis in extracts from cells expressing FLAG-Stx17 and WT IRGM or GFP-IRGM^{S47N} in 293T cells. In IP blots, GFP-IRGM and GFP sections were cropped to avoid IgG bands. **(E)** CoIP analysis of interaction between GFP-IRGM WT or GFP-IRGM^{S47N} with Beclin1. **(F)** Left: GFP-IRGM intensities IPs/input ratio. Right: IP/input ratios of Beclin1. **(G)** CoIP analysis using GFP-Stx17 and FLAG-IRGM (WT) or FLAG-IRGM^{Kmut} in 293T cells. WB, Western blot. **(H)** CoIP analysis of interaction between FLAG-IRGM WT or FLAG-IRGM^{Kmut} with Beclin1. **(I)** Left: IP/input ratios of GFP-Stx17. Right: IP/input ratios of Beclin1. Data indicate means and SEM. **, $P < 0.01$; †, $P \geq 0.05$ ($n = 3$) *t* test. **(J)** GST pulldown analysis using radiolabeled [^{35}S]Myc-Stx17 and GST-IRGM.

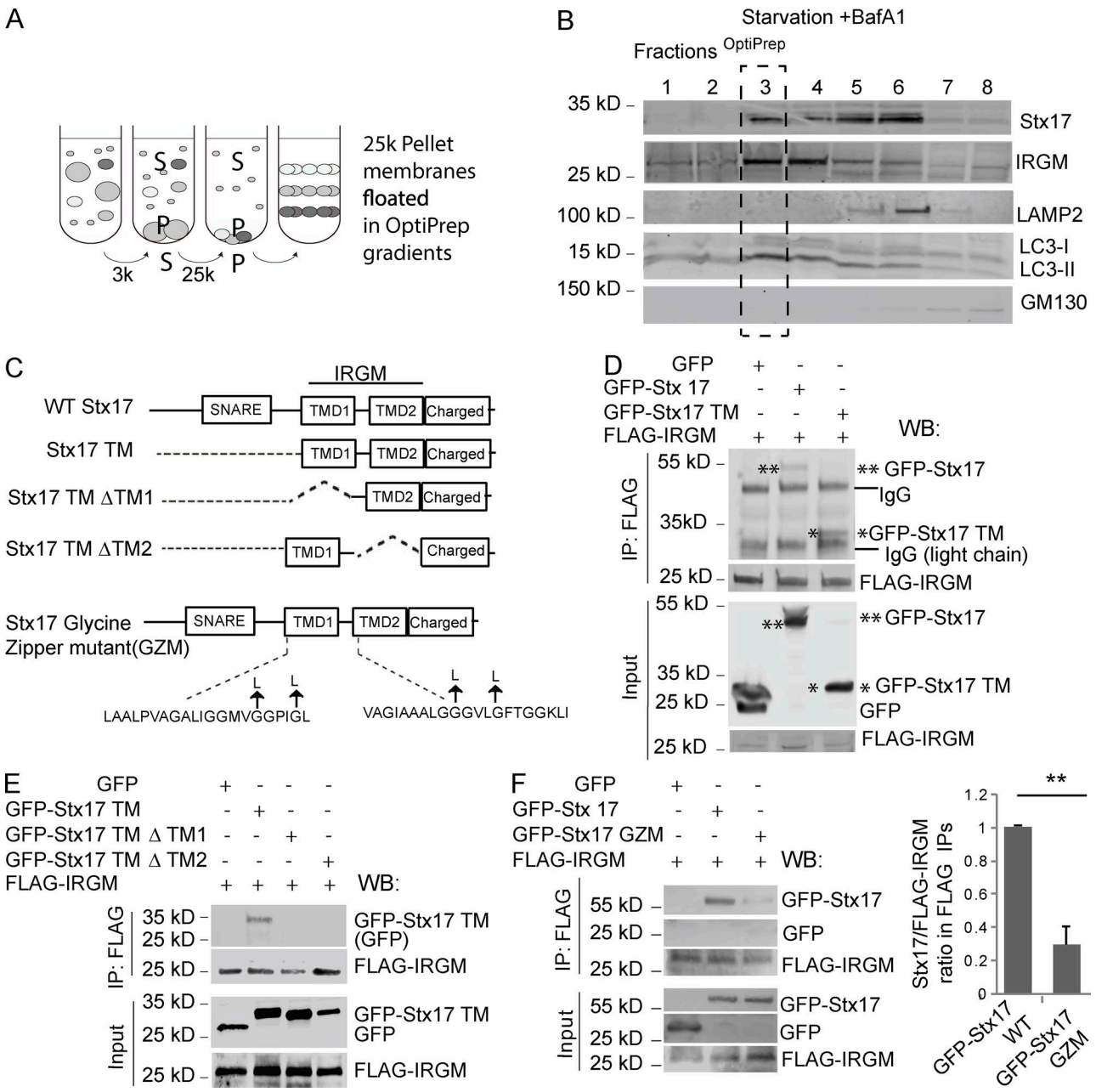

Figure 4. **IRGM cofractionates with Stx17 on membranes and binds to a region required for Stx17 autophagosomal localization. (A)** Schematic showing sequential fractionation by differential centrifugation and membrane flotation from the 25k pellet in OptiPrep gradients. P, pellet; S, supernatant. **(B)** Western blot (WB) analysis of proteins in membrane fractions from OptiPrep gradients (1–8 fractions, light to heavy; see the Membrane fractionation section of Materials and methods for details. **(C)** Schematic of Stx17 domains and constructs used for mapping in D and E. Charged, a region with charged residues; GZM, Gly zipper mutant disrupting TMD1–TMD2 interactions. **(D and E)** Mapping of the IRGM-interacting region in Stx17 by coIP analyses. **, GFP-Stx17 band; *, GFP-Stx17TM band; —, IgG bands in IP products. **(F)** CoIP analysis of the effects of mutations in glycine zipper motif ($GZM^{G44/48/64/68\text{-}liter}$) in Stx17 on interactions between GFP-Stx17 and FLAG-IRGM in 293T cells. In IP blots, GFP-Stx17 and GFP sections were cropped to avoid IgG bands. Data indicate means ± SEM of intensities normalized to IP input as indicated. **, $P < 0.01$ ($n = 3$) *t* test.

zipper-like (GZM) motifs, and this structure is essential for Stx17 to insert into autophagic membranes (Fig. 4 C; Itakura et al., 2012). A truncated Stx17 derivative (Stx17 TM) containing both TMDs previously characterized as sufficient for delivery of Stx17 to autophagosomes (Itakura et al., 2012) retained IRGM-binding capacity when compared with full-size Stx17 (Figs. 4 D and S3 D). We then tested truncated derivatives of Stx17 containing only the domains TMD1 and TMD2 (Fig. 4 E). When either TMD1 or TMD2 were deleted within Stx17 TM, IRGM no longer coimmunoprecipitated with these Stx17 derivatives (Fig. 4 E). IRGM showed diminished interaction with the $Stx17^{G244/G248/264/268L}$ mutant (Stx17GZM; Fig. 4 F), known to disrupt the glycine zipper packing interface between the two TMDs (Itakura et al., 2012). Thus, IRGM interacts with the Stx17 regions required for its insertion into membranes possibly while they are still accessible or not fully buried in lipid bilayers of the autophagosome.

IRGM assists recruitment of Stx17 to autophagosomes

We next tested whether IRGM contributes to the recruitment of Stx17 to LC3$^+$ autophagosomes. When IRGM was knocked down, Stx17 was no longer recruited to LC3$^+$ organelles in cells induced for autophagy by starvation as observed by confocal microscopy and quantification of the quality of colocalization (Fig. 5 A). This was further quantified in a time-course analysis by HC imaging and determining of percent overlaps between Stx17 and LC3 profiles (Fig. S3 E); in these quantifications, Stx17 was used as the denominator when determining percent overlap with LC3B profiles to avoid the potential effects of IRGM knockdowns on total LC3 puncta. We also tested the effects of IRGM knockdown in cells transfected with Stx17LIR**, and we observed that IRGM may play a dominant role in the placement of Stx17 on autophagosomes because IRGM knockdown diminished overlap between LC3 profiles and Stx17 to the baseline levels for both Stx17WT or Stx17LIR** at the 15-min time point in the time course experiment (Fig. S3 E). Consistent with these observations, GFP-IRGM expression increased LC3-II/LC3-I ratios in complexes with Stx17 relative to overall LC3-II/LC3-I ratios in cells (Fig. 5 B).

To test whether IRGM played a role in Stx17 recruitment to membranes, we examined levels of Stx17 in 25K membrane pellet fractions (positive for LC3; Ge et al., 2013). Stx17 detectable in 25K membrane pellets was decreased by knocking down IRGM (Fig. 5 C). IRGM knockdowns caused redistribution of Stx17 from membranes pelleted at 100,000 *g* (100K) to 100K supernatants (Fig. 5 D), albeit, as a control, levels of Stx17 in total cell lysates were not affected by knocking down IRGM (Fig. 5 D). Thus, IRGM is required for efficient Stx17 recruitment to autophagic membranes.

IRGM interacts with mAtg8s

How might IRGM recruit Stx17 to the autophagosome? We hypothesized that IRGM too recognized LC3/mAtg8s on these organelles, thus pivoting recruitment of Stx17 to the autophagosome. All mAtg8s were found in coIPs with FLAG-IRGM complexes (Fig. S3 F). GST pulldowns showed that IRGM interacted directly with mAtg8s (Fig. 6 A).

We analyzed IRGM for the presence of potential LIR sequences based on established criteria (Birgisdottir et al., 2013) and found three putative motifs (L1, L2, and L3) predicted to be exposed on the protein surface using the known crystal structure of an IRGM homologue 1TQ6 (Irga6; IIGP1; NCBI Gene ID 60440; Fig. S4, A–C). IRGM peptide arrays, using the previously reported strategy for mapping potential LIRs (Mandell et al., 2014; Kimura et al., 2015), indicated that L1–L3–containing peptides bound mAtg8s (Fig. S4 D). Another binding site was observed in peptide array blots (L4; Fig. S4 D), but the corresponding residues were predicted to be buried, so L4 was not pursued further. When we mutated the putative candidate LIRs, IRGM and mAtg8s still associated without any detectable reduction in affinity when tested by GST pulldowns and coIPs (Fig. S4, D–I). We also observed that mutations in putative LIRs in IRGM did not affect its binding to Stx17 (Fig. S4 H).

We next tested whether the LIR docking site (LDS; Behrends et al., 2010) in LC3B mattered for IRGM binding and found that the LC3B LDS mutant (F52A/L53A; Behrends et al., 2010) fully retained its IRGM-binding capacity (Fig. 6 B). Thus, the following model emerges whereby IRGM interacts with Stx17 and IRGM interacts with mAtg8s in a non–LDS–LIR mode, thus recruiting Stx17 to autophagosomes. Stx17 in turn binds to mAtg8s through conventional LIR interactions. This combination regulates recruitment of Stx17 to autophagosomes.

A model depicting the Stx17-LC3B-IRGM holocomplex, which we termed ARP, showing the details of interaction sites delineated above, is displayed in Fig. 6 C.

IRGM and SNARE assemblies with Stx17

Stx17, a Q_a-SNARE, cooperates with the Q_{bc}-SNARE SNAP-29, recruited from the cytosol, and with the R-SNARE VAMP8 on lysosomal membranes to conduct membrane fusion between autophagosomes and lysosomes (Itakura et al., 2012; Diao et al., 2015). GFP-VAMP8 coimmunoprecipitated with FLAG-IRGM (Fig. S4 J), and endogenous VAMP8 was found in coIPs of endogenous IRGM (Fig. 7 A). Knockdowns of IRGM reduced the amount of endogenous Stx17 in coIP complexes with VAMP8 (Fig. 7 B), suggesting that IRGM contributes to the assembly of Stx17 with its cognate R-SNARE involved in autophagosome–lysosome fusion (Itakura et al., 2012; Diao et al., 2015). VAMP8 and IRGM presence in common complexes was increased when autophagy was induced with pp242 (Fig. 7, C and D). Thus, IRGM interacts not only with Stx17 but it is also in complexes with the Stx17 cognate R-SNARE VAMP8 involved in autophagosome–lysosome fusion (Itakura et al., 2012; Diao et al., 2015).

Stx17 interacts (Jiang et al., 2014; Takáts et al., 2014) with the HOPS tethering complex (Balderhaar and Ungermann, 2013; Solinger and Spang, 2013), which controls the status of trans-SNARE complexes (Xu et al., 2010). GFP-IRGM coimmunoprecipitated with VPS39 and VPS33A (Fig. 7, E and F), components of HOPS shown to be in complex with Stx17 (Jiang et al., 2014). GFP-IRGM did not coIP with VPS8 (Fig. 7 G), a component of the class C core vacuole/endosome tethering (CORVET) complex, which shares core components with HOPS but functions in endosomal fusion (Balderhaar and Ungermann, 2013; Solinger and Spang, 2013). Thus, IRGM is in complexes that contain not only Q_a-SNARE Stx17 and R-SNARE VAMP8 but also include HOPS components previously reported as necessary for Stx17–VAMP8 complex detection (Jiang et al., 2014). Given that IRGM and Stx17 are also present in ARP complexes, we wondered whether once Stx17 and IRGM are in complexes with HOPS, the status of Stx17 association with mAtg8s changes. Indeed, HOPS affected levels of mAtg8 association with Stx17 as knockdown of VPS33A increased the amount of endogenous Stx17 in coIPs with GFP-LC3B (Fig. 7 H). This suggests that recruitment of Stx17 by ARP to autophagosomes may be followed by a displacement of mAtg8s from Stx17 to free its SNARE domain and make it available for interactions with its cognate R-SNARE. Alternatively, increases in Stx17-LC3 association in cells knocked down for HOPS may be indirect effects of a block in fusion and precursor accumulation. Thus, further experiments are necessary to discern between these possibilities.

Stx17 is required for control of intracellular *Mycobacterium tuberculosis*, and its interaction with IRGM is targeted by HIV protein Nef

IRGM affects *M. tuberculosis* control by autophagy (Singh et al., 2006). IRGM has been shown to regulate assembly of autophagy initiation machinery (Chauhan et al., 2015), but IRGM's effects on maturation has not been established. We

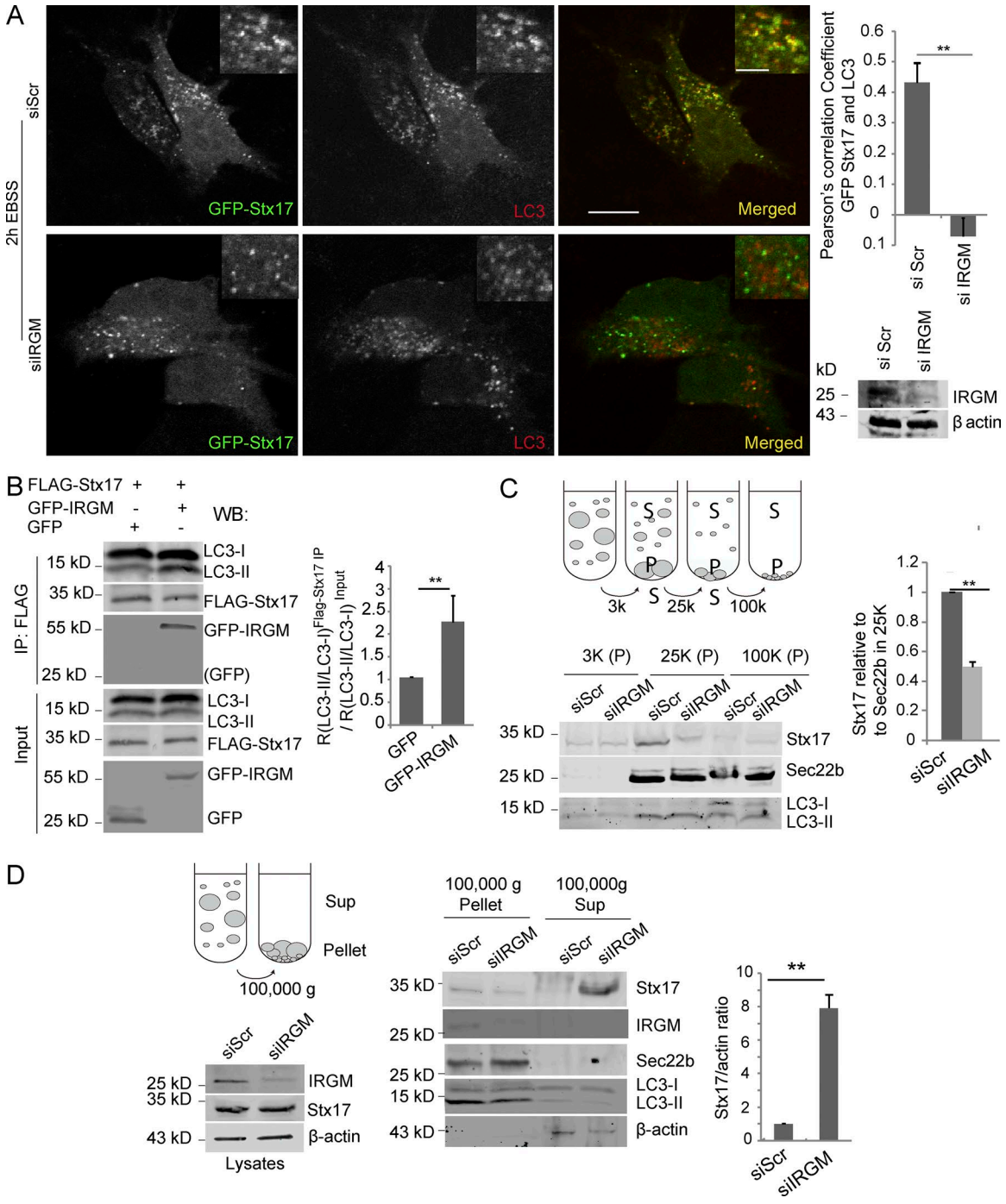

Figure 5. **IRGM recruits Stx17 to autophagosomal membranes. (A)** Left: Effects of IRGM knockdown on Stx17-LC3 colocalization. HeLa cells were knocked down for IRGM and transfected with GFP-Stx17. Bars: (main images) 5 µm; (insets) 1 µm. Right: Colocalization (Pearson's correlation coefficient) between LC3 and GFP-Stx17 analyzed by confocal microscopy. The Western blot indicates IRGM knockdown in cells used for microscopy. **(B)** CoIP analysis of IRGM overexpression effects on interactions between FLAG-Stx17 and endogenous LC3 in 293T cells. TrueBlot secondary antibody was used to avoid IgG bands. Data indicate means ± SEM of ratios between LC3-II and LC3-I intensities in FLAG-Stx17 IPs normalized to LC3-II/LC3-I ratios in cells/input. **(C)** Effects of IRGM knockdown on distribution of Stx17 in 25k pellets (schematic shows sequential differential centrifugation as in Fig. 3 A). P, pellet; S, supernatant. Right: Intensities of Stx17 normalized to Sec22b in 25k fractions. Data indicate means ± SEM of relative intensities. **(D)** Differential fractionation (schematic) and immunoblotting analysis showing effects of IRGM knockdown on relocalization of Stx17 from membranes pelleted at 100,000 *g* to 100K supernatant containing cytosol from cell extracts (293T cells). The blot below the schematic shows a comparison of Stx17 levels in total cell lysates from control and IRGM siRNA–treated cells. The graph shows quantifications of Stx17 levels normalized to actin in 100K supernatant. Data indicate means ± SEM of relative intensities. **, $P < 0.01$ ($n = 3$) *t* test.

addressed this by HC microscopy. IRGM knockdowns in HeLa cells stably expressing mRFP-GFP-LC3 (Kimura et al., 2007) indicated maturation defects (Fig. S4 K). Furthermore, IRGM knockdown reduced colocalization between autophagosomal (LC3) and lysosomal (LAMP2) markers in cells with autophagy induced by starvation in the presence of autophagy

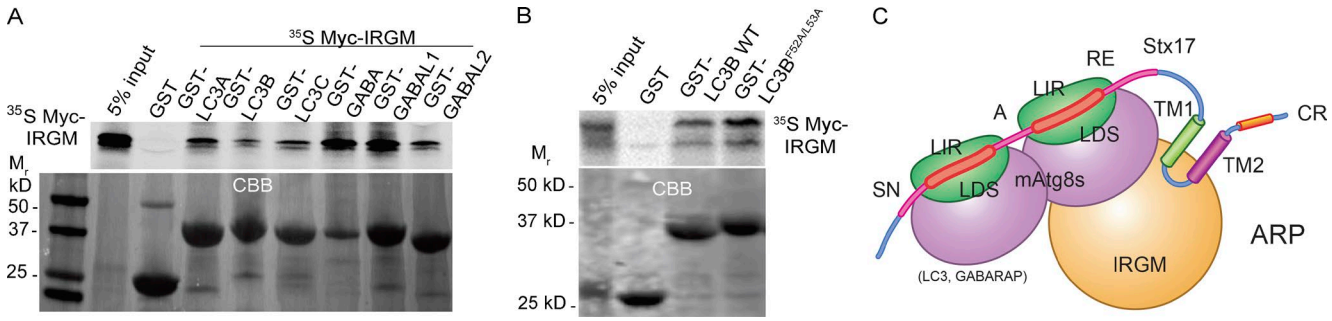

Figure 6. **IRGM directly Interacts with mATG8s. (A)** GST pulldown analysis of binding between [^{35}S]Myc-IRGM and GST-mAtg8s. **(B)** GST pulldown analysis of radiolabeled [^{35}S]Myc-IRGM with GST-LC3B WT or its LDS mutant GST-LC3B$^{F52A/L53A}$. **(C)** Model showing a summary of interactions and a depiction of identified components of the ARP. The model highlights interactions between IRGM-Stx17 (via a region overlapping with Stx17's TMDs TM1 and TM2), Stx17-LC3 (LIR–LDS type of interaction), and IRGM-LC3 (non-LDS), leading up to Stx17 recruitment to autophagosomal membranes. Stx17's LIRs are located within its SNARE domain (labeled as SN-A-RE). CR, charged residues.

flux inhibitor bafilomycin A1 to prevent degradation of LC3 and preserve it as a marker/compartment identifier (Fig. S4 L). These effects were observed during autophagic response to starvation, signifying that IRGM had an effect on events downstream of initiation stages under common autophagy-inducing conditions. We next tested the significance in control of *M. tuberculosis* of IRGM's interacting partner Stx17 researched in this study. We knocked out Stx17 in THP1 macrophages and examined their ability to control intracellular *M. tuberculosis* (Fig. 8 A). As previously shown for IRGM (Singh et al., 2006), Stx17 was required for efficient elimination of intracellular *M. tuberculosis* (Fig. 8 A), which occurs in autolysosomes (Gutierrez et al., 2004). These observations add Stx17 to the factors engaged in autophagy in the control of intracellular *M. tuberculosis*.

HIV protein Nef is known to inhibit autophagic maturation (Kyei et al., 2009; Shoji-Kawata et al., 2013), and overexpression of NEF results in the accumulation of autophagosomes at the expense of their progression to autolysosomes (Kyei et al., 2009). IRGM is a target for HIV Nef protein (Grégoire et al., 2011). The findings that IRGM interacts with Stx17 and helps its recruitment to autophagosomes as well as that it facilitates subsequent events with SNAREs and HOPS involved in autophagosomal maturation posed the question of whether Nef binding to IRGM (Grégoire et al., 2011) exerted its effects on maturation through IRGM interactions with Stx17. When Nef-GFP was coexpressed with FLAG-IRGM, less endogenous Stx17 was found in FLAG-IRGM complexes (Fig. 8 B). Earlier work (Kyei et al., 2009) has established that a Nef mutant 174DD175-to-174AA175 (Nef$^{DD\text{-}AA}$) does not inhibit autophagosomal maturation, and thus we tested whether Nef$^{DD\text{-}AA}$ associated with IRGM. In cells coexpressing FLAG-IRGM with Nef-GFP, Nef$^{DD\text{-}AA}$-GFP, or GFP, a positive coIP was found only between FLAG-IRGM and Nef-GFP but not between FLAG-IRGM and Nef$^{DD\text{-}AA}$-GFP (Fig. 8 C). When we tested the effects of the IRGM-nonbinding mutant Nef$^{DD\text{-}AA}$ on interactions between FLAG-IRGM and endogenous Stx17, the Nef$^{DD\text{-}AA}$ mutant lost the ability to interfere with IRGM-Stx17 association (Fig. 8 B). Thus, the interactions uncovered in this study between IRGM and Stx17 are targeted by the HIV protein Nef and are in keeping with the known inhibitory effects of Nef on autophagic maturation (Kyei et al., 2009; Shoji-Kawata et al., 2013).

Discussion

This study explains how Stx17, a key SNARE leading to autophagosome maturation (Itakura et al., 2012; Hamasaki et al., 2013; Tsuboyama et al., 2016), is recruited to autophagosomes as a prelude to autophagosomal–lysosomal fusion. The simplicity of this recruitment mechanism should not escape attention given that it is LC3 and other mAtg8s on autophagosomal membranes that directly bind Stx17 and IRGM in the process of Stx17 acquisition by the autophagosomes. Importantly, IRGM binds directly to the C-terminal section of Stx17 known to be required for its delivery to autophagosomes (Itakura et al., 2012; Hamasaki et al., 2013; Tsuboyama et al., 2016). IRGM in turn binds to mAtg8s such as LC3, which provides the address for the delivery of this complex to autophagosomes.

The direct binding of mAtg8s to the SNARE domain of Stx17 may play an ancillary role in increasing the fidelity of Stx17 recruitment to autophagosomes (see model in Fig. 9). It also likely plays a role in the occlusion of the SNARE domain of Stx17 and its accessibility. We predict that mAtg8s bound to LIRs within the SNARE motif of Stx17 help prevent premature engagement of Stx17 in trans-SNARE complexes. Once autophagic vesicles are ready for fusion, e.g., upon their closure, mAtg8s bound to the SNARE domain of Stx17 will have to be displaced by factors such as HOPS to allow full SNARE pairing and autophagosome–lysosome fusion. Why are mAtg8s not sufficient to recruit Stx17 to autophagosomes and additional factors needed? This may be best understood from a phylogenetic perspective. The LIRs of the type analyzed in this study are absent in *Drosophila melanogaster* Stx17, although the Stx17 LIR WETL is conserved from humans to fish, and thus modulation of recruitment and activation of Stx17 through an mAtg8-dependent mechanism probably came later on in evolution.

The same molecular entities involved in the recruitment of Stx17 to autophagosomes play a role in subsequent regulatory processes leading up to autophagosome–lysosome fusion. The engagement of the Stx17-cognate R-SNARE VAMP8 is influenced by IRGM. This complements the assembly of these SNAREs with the Q_{bc}-SNAREs completing the four-helix SNARE bundle, dictated by other specialized factors including EPG5 (Wang et al., 2016), PLEKHM1 (McEwan et al., 2015; Nguyen et al., 2016; Wijdeven et al., 2016), and posttranslational modifications (Guo et al., 2014).

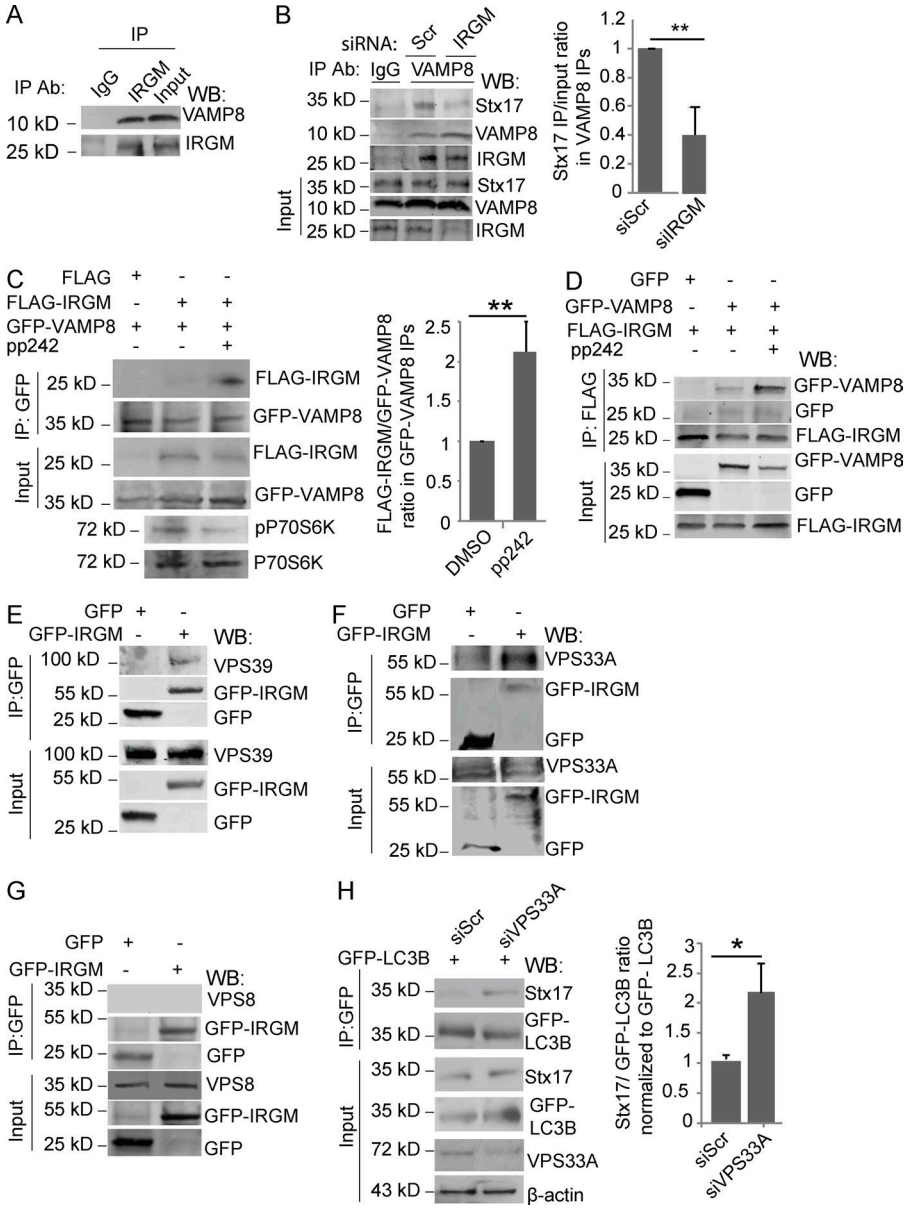

Figure 7. **IRGM relationship with R-SNARE and HOPS complexes participating in autophagosome–lysosome fusion. (A)** CoIP analysis between endogenous VAMP8 and IRGM in 293T cells. **(B)** 293T cells were knocked down for IRGM, and endogenous VAMP8 and Stx17 interactions were analyzed by coIP. Right: Quantifications of Stx17 IP/input ratio in VAMP8 IPs. **(C)** CoIP analysis of FLAG-IRGM and GFP-VAMP8 interactions upon induction of autophagy with pp242 in 293T cells; pp242 activity was monitored by pP70S6K phosphorylation (bottom). Right: FLAG-IRGM intensities normalized to GFP-VAMP8 in GFP-VAMP8 IPs. Data indicate means ± SEM of normalized intensities. **, $P < 0.01$ ($n = 3$) *t* test. **(D)** CoIP analysis of pp242 effect on interactions between FLAG-IRGM and GFP-VAMP8 in 293T cells. In IP blots, GFP-VAMP8 and GFP sections were cropped to avoid IgG bands. **(E and F)** CoIP analysis of GFP-IRGM and HOPS subunits (endogenous VPS39 and VPS33A) in 293T cells. In E, IP blots for GFP-VAMP8 and GFP sections were cropped to avoid IgG bands. In F, TrueBlot secondary antibody was used to avoid IgG bands. **(G)** Analysis GFP-IRGM IPs for presence of VPS8 (CORVET subunit) in 293T cells. **(H)** Analyses of effects of VPS33A knockdown on interactions between GFP-LC3B and endogenous Stx17. Data indicate means ± SEM of intensity ratios (normalization to GFP-LC3B in IP). *, $P < 0.01$ ($n = 3$) *t* test. WB, Western blot.

Several recent studies have addressed a role of the ATG conjugation machinery and mAtg8s in the context of Stx17 function and effects on autophagosomal maturation (Nguyen et al., 2016; Tsuboyama et al., 2016). Tsuboyama et al. (2016) reported that in Atg3-knockout (KO) cells, Stx17 puncta formation was severely reduced down to 30% of WT cell levels in addition to a delay in the lysis of the inner autophagosomal membrane and presumably of the captured cargo. Our observations explain the 70% loss of Stx17 during autophagosomal maturation in the absence of the Atg conjugation machinery. This is supported by our findings of the lack of Stx17 recruitment in cells expressing $Atg4B^{C74A}$, a dominant-negative mutant sequestering mAtg8s (Fujita et al., 2008). Our data cannot account for the remaining Stx17 dots observed by Tsuboyama et al. (2016), but these could be a result of the presence of Stx17 on mitochondrial-derived vesicles (McLelland et al., 2016) and, as reported earlier, Stx17's presence on reticulate and mitochondrial profiles (Itakura et al., 2012), its reported anchoring in the smooth ER (Steegmaier et al., 1998, 2000), and additional roles that Stx17 may play at the mitochondria–ER contact sites (Hamasaki et al., 2013; Arasaki et al., 2015). Collectively, our findings are congruent with the role of mAtg8s in autophagosomal–lysosomal fusion as shown by major delays in maturation in the Atg3-KO cells (Tsuboyama et al., 2016) and absence of maturation in mAtg8-all/hexa–KO mutant cells (Nguyen et al., 2016).

The mAtg8s binding to the SNARE domain of Stx17 postulate both a SNARE domain occlusion and that a timely dissociation of mAtg8s right before the four-helix bundle of the trans-SNARE complexes is to be formed to drive the autophagosome–lysosome fusion. This may play a regulatory role in addition to the contributory role of mAtg8s in Stx17 recruitment. Other SNARE interactors and binders to SNARE domains are known to play such roles. For example, Lürick et al. (2015) have shown that Vps33 of the HOPS complex interacts with the Habc domain of Vam7 SNARE in yeast, albeit not with the SNARE domain, to regulate the role of SNAREs in fusion. More recent work on Vps33 with Vam3 and Nyv1 by Baker et al. (2015) shows crystal structures of partially (but still not fully) ordered SNARE domains of SNAREs with HOPS Vps33 as a prelude to the formation of a four-helix bundle. According to

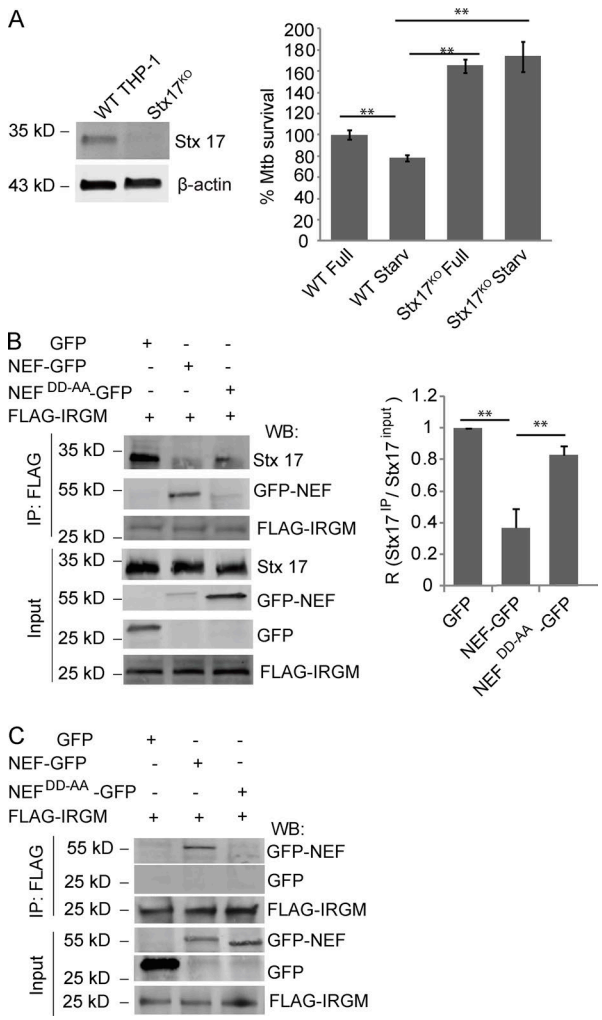

Figure 8. **Stx17 and IRGM as effectors and targets for infectious agents.** **(A)** *M. tuberculosis* survival assay in WT and Stx17^{KO} THP-1 cells. Left: Western blot (WB) showing Stx17 KO in THP-1 cells. Right: Percent survival of *M. tuberculosis* in WT and CRISPR (lentivirus) Stx17^{KO} THP-1 cells differentiated with 50 nM PMA and incubated in either full media or EBSS for 2 h. Data indicate means ± SEM (percentage of remaining colony-forming units relative to WT THP-1 cells incubated in full medium). **(B)** CoIP comparison of NEF effects (WT NEF vs. mutant NEF$^{174DD-AA175}$) on association between FLAG-IRGM and endogenous Stx17 in 293T cells. Right: Quantifications from three independent experiments, with only one blot shown. Data indicate means ± SEM of normalized intensities. **, $P < 0.01$ ($n = 3$) ANOVA. **(C)** CoIP analysis of FLAG-IRGM with NEF-GFP (WT vs. NEF$^{174DD-AA175}$ mutant) in transfected 293T cells. In IP blots, GFP-NEF and GFP sections were cropped to avoid IgG bands.

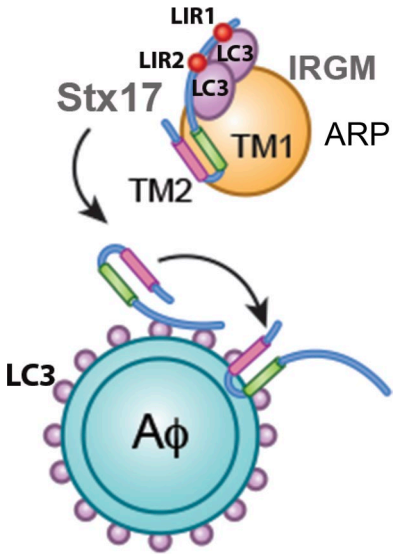

Figure 9. **Overall model of Stx17 recruitment to autophagosomes.** A simplified model of how autophagosome recognition particle (ARP) delivers Stx17 to autophagosomes. First, ARP (IRGM; Stx17 with its LIRs bound by LC3 or other mAtg8s plus potential other components) allows the insertion of Stx17 into the autophagosomal membrane through exchange interactions with LC3/mAtg8s on autophagosomes. Then, the SNARE domain, occupied by LC3/mAtg8s, is released in a controlled fashion (e.g., HOPS [see Fig. 6 C] along with other key factors such as EPG5, etc.; not depicted), allowing pairing with other cognate SNAREs.

that study, SNARE domains can form partially structured complexes with Vps33. However, these structures with HOPS are formed only after the SNAREs are delivered to HOPS, whereas our study suggests that Stx17–mAtg8 interactions occur before such complexes could even form. It is possible that HOPS help displace mAtg8s from Stx17 to permit SNARE fusion, in keeping with our finding that VPS33A knockdown increases LC3B association with Stx17.

Nguyen et al. (2016) found that inactivation of mAtg8s prevented autophagosomal maturation, in keeping with our principal findings and with our observations that dominant-negative Atg4B^{C74A} (Fujita et al., 2008), which blocks lipidation of all mAtg8s, prevented Stx17 recruitment to membranes. We observed a role for Stx17 in defense against intracellular *M. tuberculosis*. Autophagic removal of bacteria and mitochondria has been likened to each other (Deretic, 2010), and experimental evidence in support of shared pathways exists (Manzanillo et al., 2013; Franco et al., 2017) However, Nguyen et al. (2016) reported that Stx17 appears not to significantly affect degradation of mitochondria through autophagy, albeit this is in direct variance with the study by Yamashita et al. (2016) but is in keeping with a study by McLelland et al. (2016). Although some of the systems (e.g., Parkin) have been implicated in both mitophagy and xenophagy (Deretic, 2010; Manzanillo et al., 2013), there nevertheless could be differences at the terminal stages of these pathways.

IRGM interacts directly with Stx17. Other factors reported to affect Stx17-based autophagosome–lysosome fusion show some similarities but also differ significantly from IRGM. For example, the previously reported autophagosome–lysosome fusion modulator EPG5 does not bind directly to Stx17 (Wang et al., 2016). Instead, it assists the once-assembled Q_{abc}-SNARE complex (Stx17–SNAP-29) in completing a four-helix SNARE bundle, with the R-SNAREs VAMP7/VAMP8 located on endosomes/lysosomes and enhanced by direct EPG5 interactions with VAMP7/8. EPG5, like IRGM, binds to LC3 but through a LIR motif, and this may help bridge autophagosomes with lysosomes. However, the nature of LC3 interactions is different between EPG5 and IRGM, because IRGM binds LC3 and other mAtg8s independently of LIR–LDS interaction; this independence from LIRs/LDS enables IRGM to recruit Stx17 directly to autophagosomes without interfering with Stx17–LC3 interactions. Another factor, PLEKHM1 (McEwan et al., 2015), an effector of Rab7 on late endosomal/lysosomal compartments, interacts with mAtg8s (similarly to EPG5 through LIR interactions) and is found in complexes with Stx17, SNAP-29, and HOPS. PLEKHM1 has interesting properties as it also forms

complexes with Vti1b, another Q_b-SNARE for which a function in autophagosomal maturation is yet to be determined (McEwan et al., 2015). Another Rab7 effector acting from lysosomes, RILP, functions in parallel to PLEKHM1, with both of these effectors interacting with endosomally/lysosomally located HOPS during autophagosomal–lysosomal fusion (Wijdeven et al., 2016). The localization of PLEKHM1, RILP, and their regulator Rab7 on lysosomes argues against them being direct recruiters of Stx17 to autophagosomes but rather acting as factors enabling important subsequent fusion complex formation and events. Thus, IRGM is not redundant with but rather complementary to other known specialized factors including PLEKHM1 (McEwan et al., 2015; Nguyen et al., 2016; Wijdeven et al., 2016) and EPG5 (Wang et al., 2016). Nevertheless, we cannot exclude existence of other alternative chaperones or regulators that act similarly to IRGM by binding the C-terminal region of Stx17 and mAtg8s, thus recruiting Stx17 to nascent autophagosomes. Of relevance in this context are also certain phylogenetic aspects of LIRs in Stx17 and IRGM during evolution. Although immunity-related GTPases are usually considered to be a prolific family of proteins in vertebrates, lower species may not always have recognizable or annotated homologues. Therefore, the IRGM-based ARP complex described in our study may not be the only recruiter/chaperone to facilitate Stx17 delivery to autophagosomes, although *Caenorhabditis elegans* has an IRGM-like protein, EXC-1, thus far implicated only in endosomal recycling (Grussendorf et al., 2016).

The role of SNAREs in the autophagosomal system is receiving increasing attention, although the various participants are not unequivocally aligned along a clear pathway. The role of SNAREs in autophagy has been studied in yeast (Liu et al., 2016), *C. elegans* (Guo et al., 2014), *Drosophila* (Takáts et al., 2013, 2014), and mammals (Itakura et al., 2012; Diao et al., 2015; Wang et al., 2016). The principles of SNARE-catalyzed fusion between apposing membranes by forming a four-helix bundle require participation of one Q_a-SNARE, one Q_{bc}- or separate Q_b plus Q_c-SNAREs on the same membrane, and one R-SNARE on the apposing membrane to be fused (Jahn and Scheller, 2006). Multiple SNAREs have been implicated in the autophagosomal pathway. This includes formation of autophagosomal precursors derived from the plasma membrane and endosomal compartments: the Q_a SNARE Stx7, Q_b SNARE Vti1b, Q_c SNARE Stx8, and R-SNAREs VAMP7 and VAMP8. As already introduced, a number and possible excess (in terms of SNARE pairing) of SNAREs have been reported as playing direct or indirect roles in autophagolysosomal maturation: the Q_a SNAREs Stx7 and Stx17 (Itakura et al., 2012), the Q_b SNARE Vti1b (Furuta et al., 2010; Itakura et al., 2012; McEwan et al., 2015), the Q_{bc} SNAREs SNAP-29 (Itakura et al., 2012; Diao et al., 2015; Wang et al., 2016) and SNAP-25 (Wang et al., 2016), and the R-SNAREs VAMP7 and VAMP8 (Furuta et al., 2010; Itakura et al., 2012; Wang et al., 2016). In secretory autophagy, which terminates not in a fusion of autophagic organelles with lysosomes but in an exocytosis-like process, a completely different set of SNAREs has been implicated: the Q_a SNAREs Stx3 and Stx4, the Q_{bc}-SNAREs SNAP-23 and SNAP-29, and the R-SNARE Sec22b (Kimura et al., 2017). Sec22b and syntaxin 5 have also been reported as affecting autolysosomal degradative capacity but are assumed to have indirect effects via delivery of lysosomal enzymes through the constitutive secretory pathway (Renna et al., 2011). Furthermore, in yeast, the SNARE participants in autophagosome–vacuole (the single yeast lysosome) fusion appear to be oriented differently than in mammalian cells: the yeast R-SNARE (Ykt6) is on the autophagosome rather than on the late endosomes/lysosomes as found in mammals (e.g., VAMP7/VAMP8), and the Q_a- and Q_b-SNAREs Vam3 and Vti1 are on the vacuole/lysosome rather than on the autophagosome (Liu et al., 2016) as found in mammals (Stx17). These variations and apparent discrepancies require further investigations, as multiple rounds of fusion between maturing autophagosomes with lysosomes in mammalian cells might obscure the initial SNARE pairing while enabling subsequent rounds of fusions, as observed in mammalian cells (Tsuboyama et al., 2016).

In summary, IRGM and mAtg8s cooperate in the recruitment of Stx17 to autophagosomes in important physiological contexts of relevance for tuberculosis and HIV infections. The system described in this study may not only recruit and regulate Stx17 but also may contribute to the cycling of Stx17 onto and off of autophagosomal/autolysosomal organelles, a phenomenon already observed (Itakura et al., 2012). We predict that the relationships uncovered in this study represent an IRGM GTPase– and LC3 lipidation–dependent cycle and likely involve additional signaling inputs from upstream sensors and regulators. We see IRGM and mAtg8s as executors of such signaling inputs that both recruit or sequester Stx17 and keep inaccessible or accessible the SNARE domain of Stx17 as needed for pairing with other SNAREs. The positioning of the two Stx17s' LIRs to overlap with its SNARE domain is a strategic location, making it open for the formation of the four-helix SNARE complexes upon delivery to appropriate membranes and under appropriate signaling inputs.

Materials and methods

Antibodies and reagents

The following antibodies and dilutions were used: Stx17 (1:1,000 [Western blot; WB]; rabbit polyclonal; HPA001204; Sigma-Aldrich); Flag (used at 0.5 µg/ml and 1:1,000 for WB; mouse monoclonal; F1804; Sigma-Aldrich); LC3 (1:1,000 [WB]; rabbit anti–human LC3B polyclonal; L7543; Sigma-Aldrich); rabbit anti-LC3 (MBL PM036 [SR]); IRGM (1:500 [WB]; rabbit polyclonal; ab69494; Abcam); GFP (0.5 µg/ml [IP] and 1:4,000 [WB]; rabbit polyclonal; ab290; Abcam); mouse antiactin antibody (1:4,000; ab8226; Abcam); VPS33A (1:500 [WB]; rabbit polyclonal; ab178803; Abcam); VPS8 (1:500 [WB]; mouse monoclonal; ab57048; Abcam); Sec22b (1:1,000 [WB]; rabbit polyclonal; 116676; Abcam); VPS39 (1:500 [WB]; rabbit polyclonal; ab107570; Abcam); TOM20 (1:250 [immunofluorescence; IF]; rabbit polyclonal; ab78547; Abcam); VAMP8 (1:1,000 [WB]; rabbit monoclonal; ab76021; Abcam); LAMP2 (1:1,000 [WB]; 1:250 [IF]; mouse monoclonal; Developmental Studies Hybridoma Bank); GM130 (1:1,000 [WB]; mouse monoclonal 610822; BD); Beclin1 (1:500 [WB]; goat polyclonal; sc-1051; Santa Cruz Biotechnology, Inc.); GRP78/Bip (1:200 [IF]; goat polyclonal; sc10086; Santa Cruz Biotechnology, Inc.); p70s6k (1:1,000 [WB]; rabbit polyclonal; 9202; Cell Signaling Technology); streptavidin magnetic beads (50 µl/sample; 88816; Thermo Fisher Scientific); high-sensitivity streptavidin-HRP (1:1,000 [WB]; 88816-21130; Thermo Fisher Scientific); protein G Dynabeads (50 µl/IP; 88816-1003D; Thermo Fisher Scientific); GDP disodium salt (used at final concentration of 0.1 Mm; ab146529; Abcam); GppCp (GMPPCP; used at final concentration of 0.1 mM; ab146660; Abcam); bafilomycin A1 (13D02-MM; InvivoGen); and OptiPrep density gradient medium (D1556; Sigma-Aldrich).

Cell culture

HEK 293T, THP-1, and HeLa cells were obtained directly from ATCC and maintained in ATCC-recommended media. HeLa cells stably expressing mRFP-GFP-LC3B (tandem HeLa) were from D. Rubinsztein (Cambridge University; Cambridge, England, UK). WT and stably expressing dominant-negative Agt4B^{C74A} NIH3T3 cells were from T. Yoshimori (Osaka University, Osaka, Japan). THP-1 cells were differentiated with 50 nM PMA overnight before use.

Plasmids, siRNAs, and transfections

IRGM WT and its mutants IRGM^{S47N} and IRGM^{kmut} were described previously (Singh et al., 2010; Chauhan et al., 2015). To generate point mutants, constructs were first cloned into pDONR221, and mutations were induced using a site-directed mutagenesis kit (200523; Agilent Technologies). pDONR221 vectors were generated by BP cloning, and expression vectors were made by the LR reaction (Gateway; Invitrogen). Plasmid constructs were verified by conventional restriction enzyme digestion and/or by DNA sequencing. Stx17 constructs were gifts from N. Mizushima (University of Tokyo, Tokyo, Japan). LC3B and GABARAP constructs were gifts from T. Johansen (University of Tromsø, Tromsø, Norway), and the LC3B LDS mutant was provided by C. Behrends (Goethe University Medical School, Frankfurt, Germany, and Ludwig-Maximilians-Universität, Munich, Germany). Plasmids were transfected using the ProFection mammalian transfection system from Promega. All siRNAs were from GE Healthcare. Cells were transfected with 1.5 µg of siRNAs. In brief, 10^6 cells were resuspended in 100 µl of nucleofector solution kit V (Amaxa). SiRNAs were then added to the cell suspension, and cells were nucleoporated using nucleofector apparatus with program D-032. Cells were retransfected with a second dose of siRNAs 24 h after the first transfection and assayed after 48 h.

Bacterial strains and procedures

M. tuberculosis WT Erdman and its ESX-1 mutant were cultured as described previously (Chauhan et al., 2016). For intracellular mycobacterial survival assays, PMA (50 nM/ml)-differentiated THP-1 cells were infected with WT Erdman *M. tuberculosis.* Quantification of survived *M. tuberculosis* was done as described previously (Ponpuak et al., 2010). In brief, stimulated macrophages were plated in 12-well plates 12 h before infection with *M. tuberculosis* at MOI 10 for 16 h. After infection, WT and Stx17^{KO} cells were incubated in full media or in Earle's balanced salt solution (EBSS) to analyze the effect of starvation on mycobacteria survival. Cells were washed twice with PBS to remove external mycobacteria. Infected cells were then lysed to determine the number of intracellular mycobacteria at $t = 0$ by plating onto a Middlebrook agar (7H11; Sigma-Aldrich) supplemented with 0.05% Tween-80, 0.2% glycerol, and 10% OADC (oleic acid, albumin, dextrose, and catalase; BD) and grown at 37°C, or infected cells were allowed to continue growing until harvesting at $t = 16$ h for colony-forming unit analysis. Percent mycobacteria survival was calculated by dividing the number of intracellular mycobacteria at $t = 16$ h over that of $t = 0$ multiplied by 100 and relative to control cells set to 100%.

Generation of Stx17 CRISPR mutant cells

Stx17 CRISPR in HeLa and THP-1 cells was generated as follows. The lentiviral vector lentiCRISPRv2 carrying both Cas9 enzyme and a guide RNA targeting Stx17 (guide RNA target sequence, 5′-GATAGT AATCCCAACAGACC-3′) was transfected into HEK293T cells together with the packaging plasmids psPAX2 and pCMV-VSV-G at the ratio of 5:3:2. 2 d after transfection, the supernatant containing lentiviruses was collected and used to infect HeLa and THP-1 cells. 36 h after infection, the cells were treated with puromycin (1 mg/ml) for 1 wk to select Stx17-KO cells. The KO was confirmed by Western blotting.

HC microscopy

Cells were plated and studied in 96-well plates. After transfection, cells were stimulated for autophagy by incubating in EBSS for 2 h followed by fixation with 4% paraformaldehyde for 10 min. Cells were permeabilized with 0.1% saponin and blocked in 3% BSA for 30 min followed by incubation with primary antibody for 3 h and secondary antibody for 1 h. HC microscopy with automated image acquisition and quantification was performed using a Cellomics HC scanner and iDEV software (Thermo Fisher Scientific) in 96-well plates (Mandell et al., 2014); >300 cells were analyzed per well, and >10 wells of the 96-well plate were analyzed per sample. Fluorochromes used for imaging were Hoechst 33258 and Alexa Fluor 488, 568, or 647.

SR microscopy and analysis

SR imaging and analysis were done as described previously (Kimura et al., 2017). HeLa cells were plated on 25-mm round #1.5 coverslips (Warner Instruments) and allowed to adhere overnight. After fixation, cells were incubated with anti–rabbit-LC3 antibody overnight and washed with PBS followed by labeling with Alexa Fluor 647 (A21245; Invitrogen). The coverslip was mounted on an Attofluor cell chamber (A-7816; Thermo Fisher Scientific) with 1.1 ml of the imaging buffer. Imaging buffer consisted of an enzymatic oxygen-scavenging system and primary thiol: 50 mM Tris, 10 mM NaCl, 10% (wt/vol) glucose, 168.8 U/ml glucose oxidase (G2133; Sigma-Aldrich), 1,404 U/ml catalase (C9332; Sigma-Aldrich), and 20 mM 2-aminoethanethiol, pH 8. The chamber was sealed by placing an additional coverslip over the chamber, and the oxygen-scavenging reaction was allowed to proceed for 20 min at room temperature before the imaging started. Imaging was performed using a custom-built microscope controlled by custom-written software in MATLAB (MathWorks). An sCMOS camera (C11440-22CU; Hamamatsu Photonics) was used to collect SR data, and a second camera (DMK 31AU03; Imaging Source) was used for active stabilization (McGorty et al., 2013). A 647-nm laser (500 mW 2RU-VFL-P; MPB Communications Inc.) was used as the excitation laser, and a 405-nm laser (40 mW-DL5146-101S; Thorlabs) was used to accelerate the dark-to-fluorescent-state transition. The objective had an NA of 1.49 (APON 60× OTIRF; Olympus), and the filters consisted of an 835/70-nm filter (FF01-835/70-25; Semrock) for infrared stabilization emission path, a 708/75-nm filter (FF01-708/75-25; Semrock) for SR image emission path, and a 640/8-nm laser diode cleanup filter (LD01-640/8-12.5; Semrock). When imaging the first label (LC3), a brightfield reference image for each target cell was taken and saved. During the data acquisition, the 647-nm laser was used at ∼15 kW/cm^2 to take eight sets of 5,000 frames (a total of 40,000) at 100 Hz. After the dye was photobleached and then quenched with $NaBH_4$ as described previously (Valley et al., 2015), GFP-Stx17 was labeled by first blocking the cell with signal enhancer (136933; Molecular Probes; Thermo Fisher Scientific) for 30 min followed by relabeling with GFP-binding protein (A31852; Thermo Fisher Scientific) conjugated with Alexa Fluor 647 at 10 µg/ml for 1 h. For the second round of imaging, each cell was realigned using the saved brightfield reference image as described previously (Valley et al., 2015). Data were analyzed via a 2D localization algorithm based on maximum likelihood estimation (Smith et al., 2010). The localized emitters were filtered through thresholds of maximum background photon counts of 200, minimum photon counts per frame per emitter of 250, and a minimum p-value of 0.01. The accepted emitters were used to reconstruct the SR image. Each emitter was represented by a 2D Gaussian function with σ_x and σ_y equal to the localization precisions, which were calculated from the Cramér-Rao Lower Bound (CRLB).

Clustering analysis was performed with MATLAB code using clustering tools (http://stmc.health.unm.edu/tools-and-data/). 28 regions of interest (ROIs) were selected from the image. Clustering was then performed separately for each label in each ROI using the density-based DBSCAN algorithm (Daszykowski et al., 2001) choosing a maximal nearest neighbor distance of 40 nm and requiring clusters to contain at least 10 observations. In all cases, the vast majority of observations for each label in each ROI formed a single cluster. Cluster boundaries were produced via the MATLAB "boundary" function, from which cluster areas were computed. Finally, the center-to-center distances between LC3 and GFP-Stx17 cluster centroids per ROI were tabulated.

IF confocal microscopy

For IF microscopy, HeLa cells were plated onto coverslips in six-well plates. Cells were transfected with plasmids indicated in figures. Transfected cells were incubated in full media or EBSS for 2 h and fixed in 4% paraformaldehyde/PBS for 10 min followed by permeabilization with 0.1% saponin in 3% BSA. Cells were then blocked in PBS containing 3% BSA and then stained with primary antibodies according to the manufacturer's recommendation. Cells were washed three times with PBS and then incubated with appropriate secondary antibodies (Invitrogen) for 1 h at room temperature. Coverslips were then mounted using ProLong Gold Antifade Mountant (Invitrogen) and analyzed by confocal microscopy. Images were acquired on microscope (META; oil objective 63Å~/1.4; ZEISS), camera (LSM META; ZEISS), and AIM software (ZEISS). Fluorochromes used were as in HC microscopy.

APEX2 labeling and streptavidin elution

APEX2-FLAG and APEX2-FLAG-IRGM were generated using Gateway recombination cloning. Biotin labeling was done as described previously (Lam et al., 2015). In brief, 293T cells were transfected with APEX2-FLAG and APEX2-FLAG-IRGM. The next day, cells were incubated with 0.5 mM biotin phenol for 45 min followed by addition of 1 mM of H_2O_2 for 1 min. Cells were washed three times with quenching buffer (Dulbecco's PBS supplemented with 10 mM sodium ascorbate, 10 mM sodium azide, and 5 mM trolox). Cells were then lysed in lysis buffer (6 M urea, 0.3 M NaCl, 1 mM EDTA, 1 mM EGTA, 10 mM sodium ascorbate, 10 mM sodium azide, 5 mM trolox, 10% glycerol, and 25 mM Tris/HCl, pH 7.5). Protein concentrations of lysates were measured, and lysates were incubated with streptavidin beads (Thermo Fisher Scientific) for 2 h, followed by three washes with lysis buffer. Proteins were eluted by boiling beads in 2× SDS sample buffer supplemented with 2 mM biotin. Eluted samples and corresponding lysates were subjected to SDS-PAGE followed by Western blotting of target proteins.

GST pulldown assay

GST pulldown assays with in vitro–translated [^{35}S]-labeled proteins were done as described previously (Kimura et al., 2015; Chauhan et al., 2016). All GST-tagged recombinant proteins were expressed in *Escherichia coli* BL21(DE3) and/or SoluBL21 (Amsbio). GST fusion proteins were purified on Glutathione Sepharose 4 Fast-Flow beads (GE Healthcare). [^{35}S]-labeled *Myc*-tagged proteins were cotranscribed/translated in vitro using the TnT T7–coupled reticulocyte lysate system (Promega). The in vitro–translated [^{35}S]-labeled *Myc*-tagged proteins were then incubated with GST-tagged proteins in 250 µl of NETN-E buffer (50 mm Tris, pH 8.0, 100 mm NaCl, 6 mm EDTA, 6 mm EGTA, 0.5% NP-40, and 1 mm dithiothreitol supplemented with cOmplete mini EDTA-free protease inhibitor cocktail [Roche]) for 2 h at 4°C and then washed five times with 1 ml of NETN-E buffer, boiled with 2× SDS gel loading buffer, and subjected to SDS-PAGE. The separated proteins were then transferred to polyvinylidene difluoride membranes using the Trans-Blot Turbo Transfer system (Bio-Rad Laboratories). The GST-tagged proteins were detected by staining with Ponceau S, whereas the radiolabeled proteins were detected in a PharosFX imager (Bio-Rad Laboratories).

Peptide arrays

Peptide arrays were synthesized on cellulose membrane using a MultiPep automated peptide synthesizer (INTAVIS Bioanalytical Instruments AG) as described previously (Mandell et al., 2014; Kimura et al., 2015). Interaction analyses between peptide and recombinant proteins were probed by overlaying the membranes with 1 mg/ml recombinant protein, and bound proteins were detected with HRP-conjugated anti-GST antibody (clone RPN1236; GE Healthcare).

Membrane fractionation

Membrane fractionation was performed as described previously (Ge et al., 2013). HEK293T cells (10 dishes per sample) were plated in 10-cm dishes and treated with pp242 in the presence of bafilomycin A1. For sequential centrifugation cells, cells were harvested, and the pellet was resuspended in 2.7× cell pellet volume of B1 buffer (20 mM Hepes-KOH, pH 7.2, 400 mM sucrose, and 1 mM EDTA) containing protease and phosphatase inhibitors (Roche) and 0.3 mM DTT and then was homogenized by passing through a 22-G needle until 85–90% lysis was achieved (analyzed by trypan blue staining). Homogenates were subjected to sequential differential centrifugation at 3,000 *g* for 10 min, 25,000 *g* for 20 min, and 100,000 *g* for 30 min to collect the pelleted membranes (3K, 25K, and 100K, respectively) using a TLA100.3 rotor (Beckman Coulter) and a polypropylene tube. The pellets were suspended in B88 buffer (20 mM Hepes, pH 7.2, 150 mM potassium acetate, 5 mM magnesium acetate, and 250 mM sorbitol). 5× SDS loading buffer was added, and samples were boiled for 5 min and analyzed by immunoblotting. Further fractionation using membrane floatation in a sucrose step gradient followed by centrifugation in OptiPrep step gradients was performed as described previously (Ge et al., 2013). For this, 25K membrane pellets were suspended in 0.75 ml 1.25 M sucrose buffer and overlaid with 0.5 ml 1.1 M and 0.5 ml 0.25 M sucrose buffer followed by centrifugation at 120,000 *g* for 2 h; then, the interface between 0.25 M and 1.1 M sucrose (L fraction) was suspended in 1 ml of 19% OptiPrep for a step gradient containing 0.5 ml of 22.5%, 1 ml of 19% (sample), 0.9 of ml 16%, 0.9 ml of 12%, 1 ml of 8%, 0.5 ml of 5%, and 0.2 ml of 0% OptiPrep each. The OptiPrep gradient was centrifuged at 150,000 *g* for 3 h, and subsequently, eight fractions of 0.5 ml each were collected from the top. Fractions were diluted with B88 buffer, and membranes were collected by centrifugation at 100,000 *g* for 1 h. Samples were subjected to SDS-PAGE, and Western blotting for Stx17, IRGM, LC3B, LAMP2, and GM130 was done as described in the following section.

Immunoblotting and coIP assays

Western blotting and coIP were performed as described previously (Chauhan et al., 2016). For coIP, cells were transfected with 10 µg of plasmids, and cells were lysed in NP-40 buffer containing protease inhibitor cocktail (11697498001; Roche) and PMSF (93482; Sigma-Aldrich). Lysates were mixed with antibody (2–3 µg) incubated at 4°C for 4 h followed by incubation with protein G Dynabeads (Thermo Fisher Scientific) for 2 h at 4°C. Beads were washed three times with PBS and then boiled with SDS-PAGE buffer for analysis of interacting protein by immunoblotting. In some instances, rabbit TrueBlot anti–rabbit IgG HRP (18-8816-33; Rockland), which preferentially recognizes unreduced IgG, was used as a secondary antibody to avoid the 55-kD heavy chain and 23-kD light chain IgG bands.

Statistical analyses

Data are expressed as means ± SEM ($n \geq 3$). Data were analyzed with a paired two-tailed Student's *t* test or ANOVA. Statistical significance was defined as *, $P < 0.05$; **, $P < 0.01$.

Online supplemental material

Fig. S1 shows SR microscopy analysis showing colocalization between GFP-Stx17 and LC3. Fig. S2 shows how LIR mutations in Stx17 reduce its interactions with mAtg8s and how IRGM interacts with Stx17. Fig. S3 shows how IRGM interacts with Stx17 and mAtg8s and helps recruiting Stx17 to autophagosomes. Fig. S4 shows how IRGM interacts with mAtg8s in LIR-independent manner.

Acknowledgments

We thank N. Mizushima for Stx17 constructs, T. Johansen for mAtg8 GST constructs, and C. Behrends for LC3B LDS mutant.

K.A. Lidke and M.J. Wester acknowledge support from National Institutes of Health grants EB019589, GM085273, and CA118100. This work was supported by National Institutes of Health grants AI042999 and AI111935 and by a center grant P20GM121176.

The authors declare no competing financial interests.

Author contributions: V. Deretic and S. Kumar conceptualized the study, designed the experiments, and analyzed the data; S. Kumar performed majority of the experiments; A. Jain and T.-E. Rustin performed and interpreted GST pulldowns; F. Farzam, M.J. Wester, and K.A. Lidke performed and interpreted SR microscopy; J. Jia, S.W. Choi, M.H. Mudd, A. Claude-Taupin, and Y. Gu contributed experiments; and V. Deretic wrote the manuscript with S. Kumar's input.

Submitted: 6 August 2017
Revised: 12 November 2017
Accepted: 22 December 2017

References

Alemu, E.A., T. Lamark, K.M. Torgersen, A.B. Birgisdottir, K.B. Larsen, A. Jain, H. Olsvik, A. Øvervatn, V. Kirkin, and T. Johansen. 2012. ATG8 family proteins act as scaffolds for assembly of the ULK complex: sequence requirements for LC3-interacting region (LIR) motifs. *J. Biol. Chem.* 287:39275–39290. https://doi.org/10.1074/jbc.M112.378109

Arasaki, K., H. Shimizu, H. Mogari, N. Nishida, N. Hirota, A. Furuno, Y. Kudo, M. Baba, N. Baba, J. Cheng, et al. 2015. A role for the ancient SNARE syntaxin 17 in regulating mitochondrial division. *Dev. Cell.* 32:304–317. https://doi.org/10.1016/j.devcel.2014.12.011

Baker, R.W., P.D. Jeffrey, M. Zick, B.P. Phillips, W.T. Wickner, and F.M. Hughson. 2015. A direct role for the Sec1/Munc18-family protein Vps33 as a template for SNARE assembly. *Science.* 349:1111–1114. https://doi.org/10.1126/science.aac7906

Balderhaar, H.J., and C. Ungermann. 2013. CORVET and HOPS tethering complexes - coordinators of endosome and lysosome fusion. *J. Cell Sci.* 126:1307–1316. https://doi.org/10.1242/jcs.107805

Behrends, C., M.E. Sowa, S.P. Gygi, and J.W. Harper. 2010. Network organization of the human autophagy system. *Nature.* 466:68–76. https://doi.org/10.1038/nature09204

Birgisdottir, A.B., T. Lamark, and T. Johansen. 2013. The LIR motif - crucial for selective autophagy. *J. Cell Sci.* 126:3237–3247.

Chauhan, S., M.A. Mandell, and V. Deretic. 2015. IRGM governs the core autophagy machinery to conduct antimicrobial defense. *Mol. Cell.* 58:507–521. https://doi.org/10.1016/j.molcel.2015.03.020

Chauhan, S., S. Kumar, A. Jain, M. Ponpuak, M.H. Mudd, T. Kimura, S.W. Choi, R. Peters, M. Mandell, J.A. Bruun, et al. 2016. TRIMs and Galectins Globally Cooperate and TRIM16 and Galectin-3 Co-direct Autophagy in Endomembrane Damage Homeostasis. *Dev. Cell.* 39:13–27. https://doi.org/10.1016/j.devcel.2016.08.003

Daszykowski, M., B. Walczak, and D. Massart. 2001. Looking for Natural Patterns in Data. Part 1. Density Based Approach. *Chemom. Intell. Lab. Syst.* 56:83–92. https://doi.org/10.1016/S0169-7439(01)00111-3

Deretic, V. 2010. Autophagy of intracellular microbes and mitochondria: two sides of the same coin? *F1000 Biol. Rep.* 2:45. https://doi.org/10.3410/B2-45

Diao, J., R. Liu, Y. Rong, M. Zhao, J. Zhang, Y. Lai, Q. Zhou, L.M. Wilz, J. Li, S. Vivona, et al. 2015. ATG14 promotes membrane tethering and fusion of autophagosomes to endolysosomes. *Nature.* 520:563–566. https://doi.org/10.1038/nature14147

Fasshauer, D., H. Otto, W.K. Eliason, R. Jahn, and A.T. Brünger. 1997. Structural changes are associated with soluble N-ethylmaleimide-sensitive fusion protein attachment protein receptor complex formation. *J. Biol. Chem.* 272:28036–28041. https://doi.org/10.1074/jbc.272.44.28036

Fernández, A.F., and C. López-Otín. 2015. The functional and pathologic relevance of autophagy proteases. *J. Clin. Invest.* 125:33–41. https://doi.org/10.1172/JCI73940

Franco, L.H., V.R. Nair, C.R. Scharn, R.J. Xavier, J.R. Torrealba, M.U. Shiloh, and B. Levine. 2017. The Ubiquitin Ligase Smurf1 Functions in Selective Autophagy of Mycobacterium tuberculosis and Anti-tuberculous Host Defense. *Cell Host Microbe.* 21:59–72. https://doi.org/10.1016/j.chom.2016.11.002

Fujita, N., M. Hayashi-Nishino, H. Fukumoto, H. Omori, A. Yamamoto, T. Noda, and T. Yoshimori. 2008. An Atg4B mutant hampers the lipidation of LC3 paralogues and causes defects in autophagosome closure. *Mol. Biol. Cell.* 19:4651–4659. https://doi.org/10.1091/mbc.E08-03-0312

Furuta, N., N. Fujita, T. Noda, T. Yoshimori, and A. Amano. 2010. Combinational soluble N-ethylmaleimide-sensitive factor attachment protein receptor proteins VAMP8 and Vti1b mediate fusion of antimicrobial and canonical autophagosomes with lysosomes. *Mol. Biol. Cell.* 21:1001–1010. https://doi.org/10.1091/mbc.E09-08-0693

Ge, L., D. Melville, M. Zhang, and R. Schekman. 2013. The ER-Golgi intermediate compartment is a key membrane source for the LC3 lipidation step of autophagosome biogenesis. *eLife.* 2:e00947. https://doi.org/10.7554/eLife.00947

Grégoire, I.P., C. Richetta, L. Meyniel-Schicklin, S. Borel, F. Pradezynski, O. Diaz, A. Deloire, O. Azocar, J. Baguet, M. Le Breton, et al. 2011. IRGM is a common target of RNA viruses that subvert the autophagy network. *PLoS Pathog.* 7:e1002422. https://doi.org/10.1371/journal.ppat.1002422

Grussendorf, K.A., C.J. Trezza, A.T. Salem, H. Al-Hashimi, B.C. Mattingly, D.E. Kampmeyer, L.A. Khan, D.H. Hall, V. Göbel, B.D. Ackley, and M. Buechner. 2016. Facilitation of Endosomal Recycling by an IRG Protein Homolog Maintains Apical Tubule Structure in Caenorhabditis elegans. *Genetics.* 203:1789–1806. https://doi.org/10.1534/genetics.116.192559

Guo, B., Q. Liang, L. Li, Z. Hu, F. Wu, P. Zhang, Y. Ma, B. Zhao, A.L. Kovács, Z. Zhang, et al. 2014. O-GlcNAc-modification of SNAP-29 regulates autophagosome maturation. *Nat. Cell Biol.* 16:1215–1226. https://doi.org/10.1038/ncb3066

Gutierrez, M.G., S.S. Master, S.B. Singh, G.A. Taylor, M.I. Colombo, and V. Deretic. 2004. Autophagy is a defense mechanism inhibiting BCG and Mycobacterium tuberculosis survival in infected macrophages. *Cell.* 119:753–766. https://doi.org/10.1016/j.cell.2004.11.038

Hamasaki, M., N. Furuta, A. Matsuda, A. Nezu, A. Yamamoto, N. Fujita, H. Oomori, T. Noda, T. Haraguchi, Y. Hiraoka, et al. 2013. Autophagosomes form at ER-mitochondria contact sites. *Nature.* 495:389–393. https://doi.org/10.1038/nature11910

Itakura, E., C. Kishi-Itakura, and N. Mizushima. 2012. The hairpin-type tail-anchored SNARE syntaxin 17 targets to autophagosomes for fusion with endosomes/lysosomes. *Cell.* 151:1256–1269. https://doi.org/10.1016/j.cell.2012.11.001

Jahn, R., and R.H. Scheller. 2006. SNAREs--engines for membrane fusion. *Nat. Rev. Mol. Cell Biol.* 7:631–643. https://doi.org/10.1038/nrm2002

Jiang, P., T. Nishimura, Y. Sakamaki, E. Itakura, T. Hatta, T. Natsume, and N. Mizushima. 2014. The HOPS complex mediates autophagosome-lysosome fusion through interaction with syntaxin 17. *Mol. Biol. Cell.* 25:1327–1337. https://doi.org/10.1091/mbc.E13-08-0447

Khaminets, A., C. Behl, and I. Dikic. 2016. Ubiquitin-Dependent And Independent Signals In Selective Autophagy. *Trends Cell Biol.* 26:6–16. https://doi.org/10.1016/j.tcb.2015.08.010

Kimura, S., T. Noda, and T. Yoshimori. 2007. Dissection of the autophagosome maturation process by a novel reporter protein, tandem fluorescent-tagged LC3. *Autophagy.* 3:452–460. https://doi.org/10.4161/auto.4451

Kimura, T., A. Jain, S.W. Choi, M.A. Mandell, K. Schroder, T. Johansen, and V. Deretic. 2015. TRIM-mediated precision autophagy targets cytoplasmic regulators of innate immunity. *J. Cell Biol.* 210:973–989. https://doi.org/10.1083/jcb.201503023

Kimura, T., M. Mandell, and V. Deretic. 2016. Precision autophagy directed by receptor regulators - emerging examples within the TRIM family. *J. Cell Sci.* 129:881–891. https://doi.org/10.1242/jcs.163758

Kimura, T., J. Jia, S. Kumar, S.W. Choi, Y. Gu, M. Mudd, N. Dupont, S. Jiang, R. Peters, F. Farzam, et al. 2017. Dedicated SNAREs and specialized TRIM cargo receptors mediate secretory autophagy. *EMBO J.* 36:42–60. https://doi.org/10.15252/embj.201695081

Kyei, G.B., C. Dinkins, A.S. Davis, E. Roberts, S.B. Singh, C. Dong, L. Wu, E. Kominami, T. Ueno, A. Yamamoto, et al. 2009. Autophagy pathway intersects with HIV-1 biosynthesis and regulates viral yields in macrophages. *J. Cell Biol.* 186:255–268. https://doi.org/10.1083/jcb.200903070

Lam, S.S., J.D. Martell, K.J. Kamer, T.J. Deerinck, M.H. Ellisman, V.K. Mootha, and A.Y. Ting. 2015. Directed evolution of APEX2 for electron microscopy and proximity labeling. *Nat. Methods.* 12:51–54. https://doi.org/10.1038/nmeth.3179

Liu, X., K. Mao, A.Y. Yu, A. Omairi-Nasser, J. Austin II, B.S. Glick, C.K. Yip, and D.J. Klionsky. 2016. The Atg17-Atg31-Atg29 Complex Coordinates with Atg11 to Recruit the Vam7 SNARE and Mediate Autophagosome-Vacuole Fusion. *Curr. Biol.* 26:150–160. https://doi.org/10.1016/j.cub.2015.11.054

Lürick, A., A. Kuhlee, C. Bröcker, D. Kümmel, S. Raunser, and C. Ungermann. 2015. The Habc domain of the SNARE Vam3 interacts with the HOPS tethering complex to facilitate vacuole fusion. *J. Biol. Chem.* 290:5405–5413. https://doi.org/10.1074/jbc.M114.631465

Mandell, M.A., A. Jain, J. Arko-Mensah, S. Chauhan, T. Kimura, C. Dinkins, G. Silvestri, J. Münch, F. Kirchhoff, A. Simonsen, et al. 2014. TRIM proteins regulate autophagy and can target autophagic substrates by direct recognition. *Dev. Cell.* 30:394–409. https://doi.org/10.1016/j.devcel.2014.06.013

Manzanillo, P.S., J.S. Ayres, R.O. Watson, A.C. Collins, G. Souza, C.S. Rae, D.S. Schneider, K. Nakamura, M.U. Shiloh, and J.S. Cox. 2013. The ubiquitin ligase parkin mediates resistance to intracellular pathogens. *Nature.* 501:512–516. https://doi.org/10.1038/nature12566

McEwan, D.G., D. Popovic, A. Gubas, S. Terawaki, H. Suzuki, D. Stadel, F.P. Coxon, D. Miranda de Stegmann, S. Bhogaraju, K. Maddi, et al. 2015. PLEKHM1 regulates autophagosome-lysosome fusion through HOPS complex and LC3/GABARAP proteins. *Mol. Cell.* 57:39–54. https://doi.org/10.1016/j.molcel.2014.11.006

McGorty, R., D. Kamiyama, and B. Huang. 2013. Active Microscope Stabilization in Three Dimensions Using Image Correlation. *Opt. Nanoscopy.* 2:3. https://doi.org/10.1186/2192-2853-2-3

McLelland, G.L., S.A. Lee, H.M. McBride, and E.A. Fon. 2016. Syntaxin-17 delivers PINK1/parkin-dependent mitochondrial vesicles to the endolysosomal system. *J. Cell Biol.* 214:275–291. https://doi.org/10.1083/jcb.201603105

Mizushima, N., B. Levine, A.M. Cuervo, and D.J. Klionsky. 2008. Autophagy fights disease through cellular self-digestion. *Nature.* 451:1069–1075. https://doi.org/10.1038/nature06639

Mizushima, N., T. Yoshimori, and Y. Ohsumi. 2011. The role of Atg proteins in autophagosome formation. *Annu. Rev. Cell Dev. Biol.* 27:107–132. https://doi.org/10.1146/annurev-cellbio-092910-154005

Nguyen, T.N., B.S. Padman, J. Usher, V. Oorschot, G. Ramm, and M. Lazarou. 2016. Atg8 family LC3/GABARAP proteins are crucial for autophagosome-lysosome fusion but not autophagosome formation during PINK1/Parkin mitophagy and starvation. *J. Cell Biol.* 215:857–874.

Nishida, Y., S. Arakawa, K. Fujitani, H. Yamaguchi, T. Mizuta, T. Kanaseki, M. Komatsu, K. Otsu, Y. Tsujimoto, and S. Shimizu. 2009. Discovery of Atg5/Atg7-independent alternative macroautophagy. *Nature.* 461:654–658. https://doi.org/10.1038/nature08455

Noda, N.N., Y. Ohsumi, and F. Inagaki. 2010. Atg8-family interacting motif crucial for selective autophagy. *FEBS Lett.* 584:1379–1385. https://doi.org/10.1016/j.febslet.2010.01.018

Pankiv, S., T.H. Clausen, T. Lamark, A. Brech, J.A. Bruun, H. Outzen, A. Øvervatn, G. Bjørkøy, and T. Johansen. 2007. p62/SQSTM1 binds directly to Atg8/LC3 to facilitate degradation of ubiquitinated protein aggregates by autophagy. *J. Biol. Chem.* 282:24131–24145. https://doi.org/10.1074/jbc.M702824200

Ponpuak, M., A.S. Davis, E.A. Roberts, M.A. Delgado, C. Dinkins, Z. Zhao, H.W. Virgin IV, G.B. Kyei, T. Johansen, I. Vergne, and V. Deretic. 2010. Delivery of cytosolic components by autophagic adaptor protein p62 endows autophagosomes with unique antimicrobial properties. *Immunity.* 32:329–341. https://doi.org/10.1016/j.immuni.2010.02.009

Popelka, H., and D.J. Klionsky. 2015. Analysis of the native conformation of the LIR/AIM motif in the Atg8/LC3/GABARAP-binding proteins. *Autophagy.* 11:2153–2159. https://doi.org/10.1080/15548627.2015.1111503

Renna, M., C. Schaffner, A.R. Winslow, F.M. Menzies, A.A. Peden, R.A. Floto, and D.C. Rubinsztein. 2011. Autophagic substrate clearance requires activity of the syntaxin-5 SNARE complex. *J. Cell Sci.* 124:469–482. https://doi.org/10.1242/jcs.076489

Rhee, H.W., P. Zou, N.D. Udeshi, J.D. Martell, V.K. Mootha, S.A. Carr, and A.Y. Ting. 2013. Proteomic mapping of mitochondria in living cells via spatially restricted enzymatic tagging. *Science.* 339:1328–1331. https://doi.org/10.1126/science.1230593

Rogov, V., V. Dötsch, T. Johansen, and V. Kirkin. 2014. Interactions between autophagy receptors and ubiquitin-like proteins form the molecular basis for selective autophagy. *Mol. Cell.* 53:167–178. https://doi.org/10.1016/j.molcel.2013.12.014

Sanjuan, M.A., C.P. Dillon, S.W. Tait, S. Moshiach, F. Dorsey, S. Connell, M. Komatsu, K. Tanaka, J.L. Cleveland, S. Withoff, and D.R. Green. 2007. Toll-like receptor signalling in macrophages links the autophagy pathway to phagocytosis. *Nature.* 450:1253–1257. https://doi.org/10.1038/nature06421

Shoji-Kawata, S., R. Sumpter, M. Leveno, G.R. Campbell, Z. Zou, L. Kinch, A.D. Wilkins, Q. Sun, K. Pallauf, D. MacDuff, et al. 2013. Identification of a candidate therapeutic autophagy-inducing peptide. *Nature.* 494:201–206. https://doi.org/10.1038/nature11866

Singh, S.B., A.S. Davis, G.A. Taylor, and V. Deretic. 2006. Human IRGM induces autophagy to eliminate intracellular mycobacteria. *Science.* 313:1438–1441. https://doi.org/10.1126/science.1129577

Singh, S.B., W. Ornatowski, I. Vergne, J. Naylor, M. Delgado, E. Roberts, M. Ponpuak, S. Master, M. Pilli, E. White, et al. 2010. Human IRGM regulates autophagy and cell-autonomous immunity functions through mitochondria. *Nat. Cell Biol.* 12:1154–1165. https://doi.org/10.1038/ncb2119

Smith, C.S., N. Joseph, B. Rieger, and K.A. Lidke. 2010. Fast, single-molecule localization that achieves theoretically minimum uncertainty. *Nat. Methods.* 7:373–375. https://doi.org/10.1038/nmeth.1449

Solinger, J.A., and A. Spang. 2013. Tethering complexes in the endocytic pathway: CORVET and HOPS. *FEBS J.* 280:2743–2757. https://doi.org/10.1111/febs.12151

Steegmaier, M., B. Yang, J.S. Yoo, B. Huang, M. Shen, S. Yu, Y. Luo, and R.H. Scheller. 1998. Three novel proteins of the syntaxin/SNAP-25 family. *J. Biol. Chem.* 273:34171–34179. https://doi.org/10.1074/jbc.273.51.34171

Steegmaier, M., V. Oorschot, J. Klumperman, and R.H. Scheller. 2000. Syntaxin 17 is abundant in steroidogenic cells and implicated in smooth endoplasmic reticulum membrane dynamics. *Mol. Biol. Cell.* 11:2719–2731. https://doi.org/10.1091/mbc.11.8.2719

Takáts, S., P. Nagy, Á. Varga, K. Pircs, M. Kárpáti, K. Varga, A.L. Kovács, K. Hegedűs, and G. Juhász. 2013. Autophagosomal Syntaxin17-dependent lysosomal degradation maintains neuronal function in Drosophila. *J. Cell Biol.* 201:531–539. https://doi.org/10.1083/jcb.201211160

Takáts, S., K. Pircs, P. Nagy, Á. Varga, M. Kárpáti, K. Hegedűs, H. Kramer, A.L. Kovács, M. Sass, and G. Juhász. 2014. Interaction of the HOPS complex with Syntaxin 17 mediates autophagosome clearance in Drosophila. *Mol. Biol. Cell.* 25:1338–1354. https://doi.org/10.1091/mbc.E13-08-0449

Thurston, T.L., M.P. Wandel, N. von Muhlinen, A. Foeglein, and F. Randow. 2012. Galectin 8 targets damaged vesicles for autophagy to defend cells against bacterial invasion. *Nature.* 482:414–418. https://doi.org/10.1038/nature10744

Tsuboyama, K., I. Koyama-Honda, Y. Sakamaki, M. Koike, H. Morishita, and N. Mizushima. 2016. The ATG conjugation systems are important for degradation of the inner autophagosomal membrane. *Science.* 354:1036–1041. https://doi.org/10.1126/science.aaf6136

Valley, C.C., S. Liu, D.S. Lidke, and K.A. Lidke. 2015. Sequential superresolution imaging of multiple targets using a single fluorophore. *PLoS One.* 10:e0123941. https://doi.org/10.1371/journal.pone.0123941

Wang, Z., G. Miao, X. Xue, X. Guo, C. Yuan, Z. Wang, G. Zhang, Y. Chen, D. Feng, J. Hu, and H. Zhang. 2016. The Vici Syndrome Protein EPG5 Is a Rab7 Effector that Determines the Fusion Specificity of Autophagosomes with Late Endosomes/Lysosomes. *Mol. Cell.* 63:781–795. https://doi.org/10.1016/j.molcel.2016.08.021

Wei, Y., W.C. Chiang, R. Sumpter Jr., P. Mishra, and B. Levine. 2017. Prohibitin 2 Is an Inner Mitochondrial Membrane Mitophagy Receptor. *Cell.* 168:224–238.

Weidberg, H., E. Shvets, T. Shpilka, F. Shimron, V. Shinder, and Z. Elazar. 2010. LC3 and GATE-16/GABARAP subfamilies are both essential yet act

differently in autophagosome biogenesis. *EMBO J.* 29:1792–1802. https://doi.org/10.1038/emboj.2010.74

Wellcome Trust Case Control Consortium. 2007. Genome-wide association study of 14,000 cases of seven common diseases and 3,000 shared controls. *Nature.* 447:661–678.

Wijdeven, R.H., H. Janssen, L. Nahidiazar, L. Janssen, K. Jalink, I. Berlin, and J. Neefjes. 2016. Cholesterol and ORP1L-mediated ER contact sites control autophagosome transport and fusion with the endocytic pathway. *Nat. Commun.* 7:11808. https://doi.org/10.1038/ncomms11808

Xie, Z., U. Nair, and D.J. Klionsky. 2008. Atg8 controls phagophore expansion during autophagosome formation. *Mol. Biol. Cell.* 19:3290–3298. https://doi.org/10.1091/mbc.E07-12-1292

Xu, H., Y. Jun, J. Thompson, J. Yates, and W. Wickner. 2010. HOPS prevents the disassembly of trans-SNARE complexes by Sec17p/Sec18p during membrane fusion. *EMBO J.* 29:1948–1960. https://doi.org/10.1038/emboj.2010.97

Yamashita, S.I., X. Jin, K. Furukawa, M. Hamasaki, A. Nezu, H. Otera, T. Saigusa, T. Yoshimori, Y. Sakai, K. Mihara, and T. Kanki. 2016. Mitochondrial division occurs concurrently with autophagosome formation but independently of Drp1 during mitophagy. *J. Cell Biol.* 215:649–665. https://doi.org/10.1083/jcb.201605093

Zhang, M., S.J. Kenny, L. Ge, K. Xu, and R. Schekman. 2015. Translocation of interleukin-1β into a vesicle intermediate in autophagy-mediated secretion. *eLife.* 4:e11205. https://doi.org/10.7554/eLife.11205